

Bulges and disks in the Host Galaxies of low redshift 3CR Sources: a near-IR view of their radial brightness profiles¹

Carlos J. Donzelli^{2,3,4,5}, Marco Chiaberge^{3,6}, F. Duccio Macchetto^{3,7}, Juan P. Madrid³,
Alessandro Capetti⁸, and Danilo Marchesini⁹

ABSTRACT

We analyze the near-infrared luminosity profiles and photometric parameters of the host galaxies of 3CR radio sources with $z < 0.3$, to investigate their physical nature. Our sample includes 82 galaxies, of which 22 (27%) are FR Is and 60 (73%) are FR IIs. Using near-infrared data taken both with NICMOS onboard the Hubble Space Telescope and from the ground with the Telescopio Nazionale Galileo, we find that luminosity profiles are very well described by a single Sérsic law in 52% of the cases and for the remaining objects (48%) it is necessary to include an exponential profile, which could indicate the presence of a disk. The average bulge to disk luminosity ratio for the galaxies is $(b/d) \sim 1.1$. The analysis of the photometric parameters of the sub samples indicates that FR Is and FR IIs show rather similar bulges in terms of effective surface magnitude, effective radius, and Sérsic index. On the other hand, disks in FR Is and FR IIs hosts show, on average, different properties. Central surface magnitudes are dimmer

¹Based on observations made with the NASA/ESA Hubble Space Telescope (HST), obtained at the Space Telescope Science Institute, which is operated by the Association of Universities for Research in Astronomy, Inc., under NASA contract NAS 5-26555.

² Gemini Fellow

³ Space Telescope Science Institute, 3700 San Martin Drive, Baltimore, MD 21218, USA

⁴ IATE, Observatorio Astronómico, UNC, Laprida 854, Córdoba, Argentina

⁵ CONICET, Rivadavia 1917, Buenos Aires, Argentina

⁶On leave From INAF, Istituto di Radioastronomia, Via P. Gobetti 101, Bologna, Italy, 40126-I.

⁷ Research & Space Science Department, European Space Agency, ESTEC, Noordwijk, The Netherlands

⁸ INAF - Osservatorio Astronomico di Torino, Strada Osservatorio 20, 10025 Pino Torinese, Italy

⁹ Department of Astronomy, Yale University, New Haven, CT 06520, USA

and scale lengths are greater by a factor of 2 in FR Is when compared to FR IIs. We also estimate the black hole mass associated with each galaxy using two different methods that claim tight correlations between the black hole mass (M_{BH}) with the infrared bulge luminosity (L_{bulge}) and with the Sérsic index (n). Our data indicate that masses obtained through these two methods show a high dispersion and M_{BH} obtained through L_{bulge} are systematically higher (by a factor of ~ 3) than those obtained using n . This result may reflect the fact that for our sample galaxies we do not find any correlation between L_{bulge} and n .

Subject headings: galaxies: elliptical and lenticular - galaxies: active - galaxies: jets - galaxies: surveys - infrared: galaxies

1. Introduction

Radio galaxies are a peculiar set of galaxies which give rise to a number of questions regarding their nature: What kind of effects turn these galaxies into radio galaxies? Are these effects related to galaxy morphology or galaxy environment? What are the relations between the properties of radio galaxies and the normal galaxy population? Are these properties a result of the radio activity or vice versa? In the framework of the AGN unification scheme (Urry & Padovani 1995), radio galaxies are associated with quasars. Therefore the study of such objects plays an important role to constrain physical models of quasar evolution (Kauffmann & Haehnelt 2000), to further test the unified models, and to explore the origin of radio loudness (Blandford 2000).

Radio galaxies are usually classified into two morphological classes, edge-darkened FR I and edge-brightened FR II (Fanaroff & Riley 1974), and this dichotomy corresponds to a (continuous) transition in radio power, which occurs at $L_{178} \sim 2 \times 10^{26} \text{ W Hz}^{-1}$. In modern high resolution radio maps, FR Is are characterized by bright jets near the radio “core” (centered on the host galaxy nucleus), while FR IIs have faint jets (mostly one-sided as a result of relativistic beaming effects) coupled with bright hot spots in the lobes, which mark the location where the jet impacts the ISM.

Optical studies of low-redshift radio galaxies have shown that radio galaxies of both classes are almost invariably associated with giant ellipticals, are generally found in regions of enhanced galaxy density such as clusters or dense groups, and often show signs of interaction (e.g. Zirbel 1997, Gonzalez-Serrano et al 1993). However, some differences between FR Is and FR II seem to be present. The most striking difference is related to the emission

line properties of the two classes: while most (if not all) FR Is only show weak (narrow) emission lines, FR II can be distinguished into different sub-classes, according to their spectral properties (e.g. Laing 1994). In particular, the role of a subclass of low excitation FR II (LEG) has still to be fully established: the central engine and the environment of LEG appears very similar to that of FR Is (e.g. Chiaberge et al. 2002, Hardcastle & Worrall 2000), while the radio power and morphology are typical of FR II.

While the above topics are the subject of a number of papers, there are very few detailed studies on the photometric properties of the host galaxies of radio galaxies. Zirbel (1996a) analyzes the surface brightness profiles of the host galaxies of low-redshift powerful radio galaxies. This work suggests that FR Is exhibit a weak correlation between the size of the host galaxy and the radio power, and also leads to the conclusion that FR I and FR II inhabit a different population of host galaxies. More specifically, while FR Is are typically associated with cD galaxies, FR IIs are mostly associated with a subclass of elliptical called “N-galaxies”. In ground based images, N-class galaxies appear to have peaked radial brightness profiles, while in HST images it is clear that their peculiar profiles are explained by the presence of a bright quasar-like nucleus surrounded by a faint fuzz. Therefore, when deriving the host galaxy profiles, ground-based images are unreliable if a powerful nuclear source is present.

From an imaging study of a sample of radio-quiet quasars, radio-loud quasars and radio galaxies, Dunlop et al. (2003) conclude that spheroidal hosts become more prevalent with increasing nuclear luminosity. For nuclear luminosities $M_v < -23.5$, the hosts of both radio-loud and radio-quiet quasars are all massive ellipticals. They also suggest that the basic properties of these hosts are indistinguishable from those of quiescent, evolved, low-redshift ellipticals of comparable mass.

The aim of this paper is to provide valuable infrared photometric data of a sample of 82 3CR radio galaxies and to compare these data with that obtained at other wavelengths for both normal and radio galaxies. To achieve this goal we use both ground-based and high angular resolution HST data to properly disentangle the host galaxy from any other component related to e.g. the AGN. The layout of the paper is as follows. In Section 2 we summarize the sample selection and in Section 3 we give details of the observations, image reduction and point spread function determination. In Section 4 we present the galaxy luminosity profiles and profile fitting. In Section 5 we discuss the results and in Section 6 we analyze these results from the point of view of a different classification of the galaxies of the sample. In Section 7 the black hole mass obtained through two different methods is discussed. Finally, in Section 8 we summarize our conclusions.

2. Sample selection

The sample of galaxies we analyze belongs to the Revised Third Cambridge Catalogue (3CR) (Bennet 1962a, 1962b). The 3CR catalog (Spinrad et al. 1985) is selected at 178 MHz, it includes the brightest radio sources in the northern sky ($S_{178} > 10$ Jy) and contains radio galaxies and quasars out to redshifts of ~ 2 . Since this catalogue is selected based only on the low-frequency radio properties of the sources, it is an excellent database to study the morphology and photometric attributes of the objects without any orientation bias. We chose all 3CR sources with $z < 0.3$ with the primary goal of characterizing the radio galaxy hosts mostly free from the effects of dust. There is a total of 116 sources in the 3CR up to a redshift of 0.3, and we present here the photometric properties of 82 objects. These objects were randomly observed as part of a HST snapshot program 10173. Only 7 galaxies of the sample were observed as part of other programs. They are: 3C 84 (P 7330), 3C 264 (P 7882), 3C 293 (P 9726), 3C 305 (P 7853), 3C 317 (P 7886), 3C 338 (P 7453), and 3C 405 (P 7258). Table 1 lists the observed galaxies together with the observation date, right ascension and declination for epoch 2000, FR class (Fanaroff & Riley, 1974) and morphological classification.

We used the morphological classification from NED (Nasa/Ipac Extragalactic Database) and Zirbel (1996, Paper II). As can be noted from Table 1 many of the host galaxies (57%) still remain morphologically unclassified. Most of the galaxies for which a classification is available in the literature are ellipticals. Thirty four (72%) out of the 47 morphologically classified galaxies are reported as ellipticals, while 7 (15%) objects are classified as early spirals and 6 (13%) as N type galaxies.

3. Observations and data processing

We use two different sets of near-infrared data: HST/NICMOS and Telescopio Nazionale Galileo (TNG) data. HST data are essential to derive the radial brightness profile of galaxies located at $z > 0.1$ and particularly for those with a bright nucleus that outshines the host galaxy stellar emission. TNG images are crucial for nearby galaxies ($z < 0.1$) which in general are much larger than the NIC-2 field of view and for which a direct measure of the background level is not feasible with the HST data alone. In the following we give a brief description of the datasets and the data analysis procedures.

3.1. HST Observations

All objects in our sample were observed with NICMOS Camera 2 (NIC2) that has a field of view of $19.2'' \times 19.2''$ and a projected pixel size of $0.075''$. All images were obtained using the F160W filter (similar to the standard H band) and have the same total exposure time of 1152 seconds. For only a few exceptions exposure times were shorter. These are: 3C84, 3C264, and 3C317 for which exposure times were 640, 448, and 640 seconds respectively. A more detailed technical description of the observations can be found in Madrid et al. (2006) (hereafter M2006).

We obtained the HST/NICMOS data from the Multimission Archive at the STScI (MAST). The data was processed by standard OTFR (On The Fly Reprocessing) calibration pipeline. We performed two corrections subsequent to the calibration pipeline: the removal of the pedestal effect and the masking of the coronagraphic spot. Bad columns and bad pixels were masked out too. The pedestal effect is stochastic noise introduced during the detector readout (Noll et al., 2004). Each of the quadrants of the detector have a different offset. One in particular, appears darker when compared to the others. We remove this effect using the IRAF task PEDSUB, in the Space Telescope Science Analysis System (STSDAS). NIC2 has a hole to allow coronagraphic observations, this hole produces a spot on our images and therefore we mask this spot before image combination. Information is recovered using the 4-dither pattern used for the observations. We combine the four exposures using the Pyraf task MULTIDRIZZLE also in STSDAS (Koekemoer & Fruchter, 2002). The final image is the output of MULTIDRIZZLE, in units of $e^- s^{-1}$. During our data reduction we preserve both the original sky level and the original pixel size of $0.075''$.

For the photometric calibration of the reduced data we used the formula of Dickinson et al. (2002) to derive a Vega-normalized magnitude for F160W (NIC2). We then have $m(\text{F160W}) = -2.5 \log [\text{PHOTFNU} \times \text{CR}/f_\nu(\text{Vega})] = 22.107 - 2.5 \log (\text{CR})$, where $\text{PHOTFNU} = 1.49816 \times 10^{-6} \text{ Jy s DN}^{-1}$, and CR is the count rate in DN s^{-1} . The flux density of Vega in the F160W band for NIC2 is $f_\nu(\text{Vega}) = 1043.5 \text{ Jy}$. These magnitude units are different from the ST instrumental magnitudes used by M2006. We chose the Vega system because it is more similar to the standard ground based near-IR system, and for the F160W filter the difference between Vega-mag and ST-mag corresponds to 3.68 mag.

A visual inspection of our final images revealed that the amplifier glow effect residuals were not negligible. The amplifier glow is caused by the readout amplifier situated close to each corner of the detector, and even after the correction was applied we noted that residuals for most cases were around 10% to 20% above the background level. We trim the border of the images to obtain accurate surface photometry and eliminate the amplifier glow. The resulting final field of view is $16.5'' \times 16.5''$.

3.2. TNG data

We have used the images taken by Marchesini et al. (2005). These images were obtained with the 3.6 m Telescopio Nazionale Galileo (TNG), the Italian national facility located at La Palma Island (Spain). These observations were made in two runs on Jul. 8-12, 2000 and on Feb. 9-13, 2001. ARNICA (ARcetri Near Infrared CAmera) was used in the first run and NICS (Near Infrared Camera Spectrometer) was used in the second run. ARNICA uses a 256×256 pixel NICMOS 3 array with a pixel size of $0.35''$ and a total field of view (FoV) of $1.5' \times 1.5'$ which is more than 5 times greater than the FoV of the HST NICMOS camera 2. On the other hand, NICS uses a Rockwell 1024×1024 HgCdTe Hawaii array. NICS has two modes available, the small field mode with a pixel size of $0.13''$ and a FoV of $2.2' \times 2.2'$, and the large field mode in which the pixel size and FoV are doubled. For both ARNICA and NICS observations the K' filter was used. This filter has a central wavelength of $2.12\mu m$ and a $FWHM$ of $0.35\mu m$. For NICS the total integration times of 20 min were used, while for ARNICA total integration times ranged from 5 to 24 min depending on the source. More detailed information about the individual observations are listed in Table 3 of Marchesini et al. (2005).

3.3. Background subtraction and PSF modeling

Since suitable fitting of radial profiles at low surface brightness levels is a delicate task, we are extremely cautious in the determination of the background level and its uncertainty. First of all, most of the galaxies with $z < 0.1$ cover the whole field-of-view of HST/NICMOS, therefore the background cannot be measured directly. Furthermore, a detailed analysis of the background level for the rest of the galaxies with smaller apparent diameter (those with $z > 0.1$), shows that the background is not constant. In fact, background variations among these images can be as large as 40% or more, which makes it impossible to remove it using a common value for all images. Therefore, each image of the $z > 0.1$ galaxies are to be carefully examined in order to determine the proper background level. However, our analysis shows that, in each image, a constant value across the whole detector's field-of-view is accurate enough to remove the background. For those images where this task was possible, background removal left residuals not higher than 5%.

For galaxies with $z < 0.1$ the approach is completely different. Since we are not able to determine the background on NICMOS images given that these galaxies cover the whole chip, we use ground based K' -band images taken with the TNG. Because of the much larger field of view, these images allow us to easily determine the sky level and also to obtain ac-

curate luminosity profiles in the external regions of the galaxies. The next step is to simply determine the adequate offset in order to match the luminosity profiles obtained from the HST images with those obtained from the TNG. The matching was done in an intermediate region of the luminosity profiles, avoiding the innermost regions of the TNG profiles, where seeing effects are important, and avoiding the outermost region of the HST profiles where background effects are noticeable. We find that zero points needed to match HST profiles with TNG profiles are surprisingly constant over the observation dates and the estimated errors were less than $0.05 \text{ mag arcsec}^{-2}$. Finally, we assume that the $H - K'$ color gradient is null for our galaxies and then we subtract the adequate background level on the HST images in order to match the outermost part of the HST profiles with those obtained from the TNG images. The assumption of null color gradient is supported by the fact that we do not detect any $H - K'$ color gradient for the galaxies with $z > 0.1$, where an accurate background determination on both the TNG and the HST images is possible. Further support to this assumption is found in Möllenhoff & Heidt (2001) (hereafter M&H2001). These authors showed that in a sample of 40 bright spiral galaxies the structural parameters for both the bulge and the disk components are identical for JHK filters, within the error they estimate from the data.

PSF modeling for NIC2 is well described by Suchkov & Krist (1998) and references therein. PSF diffraction structures, such as Airy rings and spikes, grow larger with increasing wavelength and therefore one must be very cautious when using infrared images. In our case, only a few cases show a bright nuclear source which causes bright PSF diffraction patterns on the images. In order to get rid of these patterns we have used the Tiny Tim modeling software (Krist, 1993) to create suitable PSF models for each of the selected images. These models were then subtracted from the individual images. This procedure works well in most images, if larger residuals were noticed they were properly masked before any isophote fitting. Besides, during the fitting procedure we also discarded the inner 3 pixels ($0.23''$) of the obtained luminosity profiles. This additional consideration avoids any fitting contamination related to the PSF subtraction (see Section 4).

4. Luminosity profiles and fitting functions

There are numerous methods for extracting luminosity profiles. The variety includes one-dimensional analysis (Bagget et al. 1988), ellipse fitting to the isophotes of the galaxies (Héraudeau & Simien 1996) and two-dimensional analysis (Byun & Freeman 1995). At first glance our infrared images show mostly elliptical galaxies with no trace of any further structures, and in a few cases (20%) we can detect dust lanes, jets or plumes. Therefore, we are mostly working with axisymmetric structures which can be easily analyzed with azimuthal

isophote fitting. For this purpose, we use the ELLIPSE routine within STSDAS (Jedrzejewski 1987). Before extracting the galaxy profile, we carefully mask all spurious objects such as stars, and residual diffraction patterns.

In the case of two galaxies overlapping, once we obtain the luminosity profile and structural parameters (center coordinates, ellipticity, and position angle of the isophotes), we construct a model galaxy using BMODEL (within STSDAS) that is subtracted from the original image. The resulting image is then used to extract the luminosity profile of the remaining galaxy. This process is repeated several times until the luminosity profiles of both galaxies converge.

Isophote fitting was performed up to a count level of $2 \sigma_{sky}$ i.e., we stopped the fitting procedure when the isophote level is around twice the background dispersion, which corresponds to a surface magnitude of $m_{F160W} = 21.8 \text{ mag arcsec}^{-2}$ on the HST/NICMOS images. This procedure is used to derive the luminosity profiles from both the TNG and the HST images.

4.1. Profile fitting

Similarly to profile extraction, luminosity profile fitting can be done using a wide variety of functions. The most common functions are the classical de Vaucouleurs $R^{1/4}$ profile (de Vaucouleurs, 1948), the exponential profile (Freeman, 1970), and the most general Sérsic profile R^n (Sérsic, 1968). Generally, the $R^{1/4}$ profile describes very well the luminosity profile of bulges, while the exponential profile is used to fit the luminosity profile of disks. However, it was recently found that the $R^{1/4}$ function does not describe the bulge profile for many ellipticals correctly. Therefore, many authors use the more general R^n profile, as is the case for Brown et al. (2003). However, for 45% of our sample galaxies, we find that a single Sérsic profile still cannot fit the data. Therefore, we try a more general case using two Sérsic profiles in order to fit the inner and outer regions of the luminosity profiles respectively. We find that the outer profile regions are well fitted with a Sérsic index $n \sim 1$, equivalent to an exponential disk. The adopted fitting function has only 5 free parameters and can be written in the following form:

$$I(r) = I_s \exp\left[-k\left(\frac{r}{r_e}\right)^n\right] + I_0 \exp\left(-\frac{r}{r_0}\right) \quad (1)$$

In the above equation the first term corresponds to the Sérsic profile, where I_s is the intensity at $r = 0$, and r_e is the radius that encloses half of the total luminosity of the bulge (also known as the effective radius). For $n < 1$, k can be approximated (with an error smaller than 0.1%) by the relation $k = 2n - 0.324$ (Ciotti 1991). The second term corresponds to

the exponential profile, where I_0 is the central intensity and r_0 is the length scale. However, as is pointed out by de Jong et al. (2004) the exponential luminosity profile does not prove that these galaxies have real disks. Kinematic data is required to confirm the presence of a disk in any individual galaxy.

Figures 1a through 1s show the luminosity profile for all the galaxies of our sample. In these figures NICMOS data are represented by squares while data from TNG are represented by triangles. The fitting functions are also displayed for the bulge (short dashed), disk (long dashed) and the sum of both components (continuum line). The radius is in Kpc (horizontal bottom axis) and *arcsec* (horizontal upper axis).

Parameters described in the above equation were obtained using the NFIT routine within STSDAS (Schombert & Bothun 1987). The fitting procedure is carried out only in the $S/N > 2$ portion of the galaxy surface brightness profiles. This is done to exclude the regions in the faint end of the luminosity profiles, in which the error is large and the information is poor. We also excluded the inner 3 pixels ($\sim 0.20''$) of the luminosity profiles in order to avoid any contamination resulting from the PSF subtraction. The errors on the parameters are calculated following the method described by Coenda et al. (2005). Briefly, this technique consists in creating test images to which we artificially add and subtract a constant value corresponding to σ_{sky} . We then extract the new luminosity profile as explained above and we fit it with Equation 1. These newly obtained parameters give us the respective upper and lower limits for the parameters.

Intensity parameters are then converted into surface brightness, expressed in $mag\ arcsec^{-2}$ by the equation $m = -2.5\log(I)$, while units of r_e , and r_0 are converted to Kpc. Measured errors for r_e and r_0 are smaller than 15% while for m_e , and m_0 are below $0.20\ mag\ arcsec^{-2}$. Total luminosities of both the bulge and the exponential components are finally computed using the derived photometric parameters and integrating separately both terms of eq. 1 as follows:

$$L = \int_0^\infty I(r)2\pi r dr \quad (2)$$

which yields:

$$L_{bulge} = I_s r_e^2 \pi \frac{2}{nk^{2/n}} \Gamma(2/n) \quad (3)$$

for the bulge component, and

$$L_{disk} = 2\pi I_0 r_0^2 \quad (4)$$

for the exponential component. $\Gamma(2/n)$ is the gamma function. Note that eq. 2 assumes that the galaxy is face on. Therefore, the intensities in eq. 1 were corrected by inclination as in Kent (1985). Total apparent magnitudes were then converted into absolute magnitudes. Throughout this paper we assume a Hubble constant $H_0 = 71\ km\ s^{-1}\ Mpc^{-1}$ together with $\Omega_M = 0.27$ and $\Omega_\Lambda = 0.73$.

5. Results and discussion

Table 2 lists the photometric parameters obtained through the procedures described in the previous sections for all sample galaxies. Columns 1, 2, and 3 list the source name, the ellipticity and redshift, respectively. Bulge parameters m_e , r_e and n are listed in columns 4, 5, and 6, while columns 7 and 8 list disk parameters m_0 (inclination corrected) and r_0 . Finally, columns 9, 10, 11, and 12 list the bulge absolute magnitudes, disk absolute magnitudes, total galaxy magnitudes and bulge to disk ratio.

Forty three out of 82 galaxies (52%) show a single Sérsic luminosity profile type. The remaining 39 galaxies (48%) have luminosity profiles that have to be fitted with a combination of a Sérsic profile plus an exponential profile. Among FR Is, 10 out of 22 galaxies (45%) show single luminosity profiles, while 12 (55%) show bulge+disk type profiles. FR IIs, show 33 out of 60 galaxies (55%) with single Sérsic luminosity profiles, and 27 galaxies (45%) with bulge+disk type profiles. However, we also have 4 interesting cases: 3C28, 3C129.1, 3C184.1 and 3C388. These galaxies show $n > 0.75$. This is somewhat reminiscent of the so-called pseudo-bulges recently discovered in some spiral galaxies. Pseudobulges are formed through secular evolution of galaxies. In other words, the bulge is formed from disk evolution, allowing the direct formation of bulges from disks in isolated galaxies (Kormendy & Kennicutt 2004). Unfortunately, we do not have enough information, such as velocity dispersions, to confirm this possibility. 3C348 is another interesting case since this galaxy has a single Sérsic profile with $n = 0.93$ which indicates it is a bulgeless galaxy. This result is unexpected since, as was pointed out in Section 2, most of these galaxies are simply reported in the literature as ellipticals. However, it is not clear whether or not the exponential profile is the signature of a disk in all of them. To investigate if these are real disks, we have plotted in Fig. 2a-d the distribution of ellipticity e for all galaxies of the sample. We differentiate between galaxies that show a single Sérsic luminosity profiles and those that show bulge+disk luminosity profiles, and also between galaxies classified as FR I and FR II. Histograms are plotted in bins of $\Delta e = 0.05$. Galaxies that show a single luminosity profile (panel d) display a distribution in ellipticity which is rather similar to that displayed by a population of normal elliptical galaxies, which has been shown to peak at $e \sim 0.15$ (Sandage, Freeman & Stokes 1970; Ryden 1992). For such a sub-sample we obtain an average ellipticity $e = 0.18 \pm 0.08$. The average ellipticity for galaxies that also show an exponential component in their luminosity profiles (panel d dashed line) is instead $e = 0.24 \pm 0.10$. A Kolmogorov-Smirnov (K-S) test applied to these sub samples indicates that these two data sets do not have different ellipticity distributions. We also note that there are no differences between FR Is (panel b) and

FR IIs (panel c) ellipticity distributions. We obtain $e = 0.21 \pm 0.11$ and 0.20 ± 0.12 for FR I and FR II galaxies respectively.

Figure 3a shows the total absolute magnitude distribution for all galaxies of the sample. Again, we have differentiated between FR I (panel b) and FR II sources (panel c), and also between galaxies with a single Sérsic luminosity profile (d). Total luminosity distributions for all the classes look similar. For the whole sample it peaks at $M_{total} = -25.4 \pm 0.7$, while for FR I and FR II sub samples separately these values are $M_{totalFR\ I} = -25.6 \pm 0.7$ and $M_{totalFR\ II} = -25.3 \pm 0.6$, respectively. The K-S test applied to FR I and FR II data sets indicates that the magnitude distributions are not statistically different.

We have made a similar analysis for bulge and disk photometric parameters for the whole sample as well as for the FR I and FR II sub samples. The average values for the photometric parameters together with their standard deviations are listed in Table 3. FR I and FR II bulges have similar properties in terms of their photometric parameters, M_{bulge} , m_e , and r_e . The Sérsic index average value is $n = 0.40 \pm 0.18$ for FR I galaxies, while for the FR II sub sample it is $n = 0.33 \pm 0.08$. However, the K-S test indicates that the distributions of the Sérsic index for FR I and FR II are not statistically different.

FR I and FR II disks show some interesting differences. As reported in Table 3, the FR Is' scale length (r_0) is on average a factor of two larger than that of FR IIs, although the spread in r_0 is large, thus they are consistent within 1σ . Similarly, the central surface magnitude (m_0) is 0.6 mag dimmer in FR I galaxies, but again consistent with that of FR IIs within 1σ . Interestingly, the K-S tests applied to these data indicates that the m_0 and r_0 distributions are statistically different at 98% and 99.9% confidence level for FR I and FR II galaxies respectively. We also find that the mean total disk magnitudes are $M_{diskFR\ I} = -25.1 \pm 0.6$ and $M_{diskFR\ II} = -24.6 \pm 0.6$. However, in this case the K-S test does not indicate that the the distributions are statistically different.

Finally, the bulge to disk luminosity ratio is $b/d = 0.8 \pm 0.4$ for FR Is while it is $b/d = 1.3 \pm 0.8$ for FR IIs. K-S test does not indicate these data sets are statistically different.

5.1. Correlation of structural parameters

The study of correlations between photometric parameters is a good tool to understand the structure of galaxies and their evolution. Many scaling relations for galaxies have been discovered this way, such as the fundamental plane (Djorgovski & Davis 1987, Dressler et al. 1987) for elliptical galaxies and the Tully-Fisher (1977) relation for spirals.

The correlations between structural parameters for both bulges and disks obtained for our sample are plotted in Fig. 4. Empty triangles represent FR IIs while filled squares represent FR Is. Panels a and b show the effective surface magnitude (m_e) and the bulge total absolute magnitude (M_{bulge}) plotted against the logarithm of the effective radius (r_e) in Kpc. From these plots we see a clear correlation between these parameters, in the sense that large bulges have a lower effective surface magnitudes and higher total luminosities. The first correlation is the Kormendy relation (Kormendy 1977) for bulge galaxies. A linear regression applied to these data gives:

$$\begin{aligned} m_e &= 16.6(\pm 0.2) + 3.2(\pm 0.3) \log(r_e/\text{Kpc}) \\ M_{bulge} &= -23.6(\pm 0.3) - 2.0(\pm 0.4) \log(r_e/\text{Kpc}) \end{aligned}$$

The slope for the m_e vs. r_e regression is quite similar to that obtained by Veilleux et al. (2006) for a sample of 33 luminous, late stage galactic mergers and also to that obtained by Dunlop et al. (2003) for their sub sample of radio loud quasars. The m_e vs. r_e relationship for these type of galaxies shows a steeper slope to that found for normal ellipticals ~ 1.8 (Pahre, 1999).

When this analysis is only applied to FR Is we obtain:

$$\begin{aligned} m_e &= 16.7(\pm 0.3) + 2.5(\pm 0.5) \log(r_e/\text{Kpc}) \\ M_{bulge} &= -23.2(\pm 0.3) - 2.6(\pm 0.5) \log(r_e/\text{Kpc}) \end{aligned}$$

While for FR IIs we have:

$$\begin{aligned} m_e &= 16.7(\pm 0.2) + 3.4(\pm 0.4) \log(r_e/\text{Kpc}) \\ M_{bulge} &= -23.7(\pm 0.4) - 1.9(\pm 0.6) \log(r_e/\text{Kpc}) \end{aligned}$$

These results indicate that FR Is and FR IIs have similar Kormendy and M_{bulge} vs. $\log(r_e)$ relations, which is in agreement with the result of Dunlop et al. (2003). These authors find similar Kormendy relations for a sample of 13 radio-quiet quasars, 10 radio-loud quasars and 10 radio galaxies.

We also investigate the correlations for disks photometric parameters. Results are shown in Figs. 4c and 4d. Disk parameters show the same trend as seen for bulge parameters. More explicitly, large disks have a lower central surface magnitude and have higher total luminosities. However, in this case the data show a larger dispersion than that observed for the bulges. Linear regression fits applied to these data yield the following results:

$$m_0 = 16.5(\pm 0.3) + 2.0(\pm 0.5) \log(r_0/\text{Kpc})$$

$$M_{disk} = -22.8(\pm 0.2) - 2.6(\pm 0.6) \log(r_0/\text{Kpc})$$

Intriguingly, these results are similar to those obtained by M&H (2001) for the disk components of a sample of 40 bright spiral galaxies. This result could give further support to the idea that exponential profiles in these galaxies are truly due to the presence of a disk. However, as it is pointed out by de Jong et al. (2003), this exponential distribution of light might not be in a disk configuration flattened by rotation as disks of spiral galaxies are.

6. FR Is, LEGs, HEGs, and QSOs

The FR I and FR II classification is only based on the radio morphology of the source. We then chose another classification scheme which relies on the spectroscopic properties, and is more likely to reflect the physical properties of the central AGN. In particular, we adopt the scheme defined by Jackson & Rawlings (1997). They classify high and low ionization narrow-lined galaxies (HEG and LEG) on the basis of the equivalent width (EW) of the [OIII]5007 emission line and/or the [OII]/[OIII] ratio. Galaxies with [OII]/[OIII] > 1 and/or EW < 10Å are defined as LEG (Low Excitation Galaxies). Similarly, quasars (QSO) are defined as those sources for which at least one broad line has been observed. We find in our sample 22 FR Is (corresponding to 27% of the sample), 22 LEGs (27%), 24 HEGs (29%), and 13 QSOs (16%). Only two FR II objects remain unclassified (3C 277.3 and 3C 346). As we pointed out in Section 5, 55% of FRI galaxies show bulge + exponential type profiles, which is identical to the percentage obtained for LEGs. HEGs show less galaxies with bulge + exponential profiles (43%), while QSOs have only 31% of the galaxies with the exponential component. It is interesting to note that even if the FR I classification is based on the radio morphology, it is known that most, if not all, FR I galaxies are weak lined LEGs (Hine & Longair, 1979; Laing, 1994).

Summarizing, we divide our objects into the following spectral classification scheme: FR Is, LEGs, HEGs and QSOs, and we investigate the statistical properties of the host galaxies under this classification. Table 4 lists the photometric parameters for each of these galaxy classes. All of them have bulges with similar average photometric properties, and even if FR Is have on average greater Sérsic indexes ($n = 0.40$ vs. $n \sim 0.34$) the Kolmogorov - Smirnov test applied to these data does not indicate that the n distribution for FR I bulges is statistically different from that of LEGs, HEGs or QSOs.

Differences between these classes arise when we compare disk photometric parameters. FR Is have on average larger disks ($r_0 = 8.2$ Kpc) and dimmer central surface magnitude

($m_0 = 18.1$) than those of LEGs ($m_0 = 17.5$, $r_0 = 4.3$), HEGs ($m_0 = 17.5$, $r_0 = 3.6$), and QSOs ($m_0 = 17.5$, $r_0 = 4.2$). However, statistical tests applied to the m_0 distributions show that FR Is differentiate only from HEGs and QSOs (99% confidence level) and not from LEGs. Same tests applied to r_0 data of these classes reveal that FR Is have a different distribution when compared with those of LEGs, HEGs and QSOs (99% confidence level). In other words, these results are similar to those obtained in the previous section. They suggest that, from a photometric point of view, FR Is are slightly different from LEGs, and these differences become stronger when FR Is are compared to HEGs and QSOs. We also ran statistical tests comparing FR Is + LEGs to HEGs + QSOs. Results were similar to those described above but with a slightly less statistical significance (98% level). We find that FR Is + LEGs have on average $m_0 = 17.8 \pm 0.5 \text{ mag arcsec}^{-2}$ and $r_0 = 6.3 \pm 2.0 \text{ Kpc}$, while HEGs + QSOs have $m_0 = 17.5 \pm 0.4 \text{ mag arcsec}^{-2}$ and $r_0 = 3.9 \pm 1.2 \text{ Kpc}$.

7. Black hole mass vs. bulge near infrared luminosity and Sérsic index

Recent studies suggest that central super massive black holes (SMBH) reside in all galaxies with a bulge, as a result of past quasar activity (Aller & Richstone 2002, and references therein). Moreover, SMBH are claimed to be related to the host galaxy properties and therefore this implies that SMBH and galaxy formation and evolution are closely correlated. Kormendy & Richstone (1995) showed that the mass of the SMBH is correlated (with a considerable scatter) with both bulge luminosity and bulge mass. This result was later confirmed and strengthened by Magorrian et al. (1998) for a sample of nearby galaxies with kinematic data.

On the other hand, it has also been shown that M_{SMBH} correlates with the Sérsic index n (Graham et al. 2003, and references therein). These authors claim that the scatter of the $M_{SMBH} - n$ relation is equivalent to the $M_{SMBH} - \sigma$ relation (Ferrarese & Merrit, 2000; Tremaine et al 2002) and it has the additional advantage of requiring only galaxy images rather than spectra.

The superb quality of HST/NICMOS images, together with ground based information for nearby objects, allows us to determine L_{bulge} and n with high accuracy. Therefore we can estimate the black hole mass for each galaxy of the sample using both relations, and check whether the results are consistent. First of all we use the following relation with L_{bulge} . as taken from Marconi & Hunt (2003):

$$\log(M_{SMBH}) = 8.04 + 1.25 (\log(L_{Hbulge}) - 10.8)$$

where M_{SMBH} is the mass of the black hole and $L_{H-bulge}$ is the total bulge luminosity in the H band in solar units.

Secondly, we use the Graham & Driver (2006) relation:

$$\log(M_{SMBH}) = 2.68 \log(1/3n) + 7.82$$

where n is the Sérsic index as expressed in Equation 1. We estimate the mass of the central black hole M_{SMBH} using the values of M_{bulge} and n as listed in Table 2, and the results are reported in Fig. 5. In the figure, empty triangles and squares represent FR I and FR II populations, respectively. The data show a large dispersion and the results obtained through these methods differ on average by a factor of three. We also used the quadratic $M_{SMBH} - n$ relation instead of the linear one given by Graham & Driver (2006) and no major differences were observed. This result might reflect the fact that we do not find any correlation between M_{bulge} and n . As can be seen in Fig. 6, neither FR I nor FR II bulge luminosities correlate with the Sérsic index. Note that similar bulge luminosity and n distributions for FR Is and FR IIs also imply similar M_{SMBH} distribution for both sub samples.

8. Conclusions

We have analyzed the infrared photometric parameters of 82 galaxies belonging to the 3CR Catalogue. From the morphological point of view most of these galaxies are not yet classified, and classified galaxies are mostly ellipticals. Nevertheless, we find that only 43 (52%) of the galaxies have a single component luminosity profile. The remaining 39 galaxies (48%) need a second component with $n = 1$ suggesting the idea that these galaxies have an exponential disk. However, we cannot confirm this possibility without additional kinematical information. When FR Is and FR IIs are differentiated we find the following results:

- 1) Forty five percent of FR Is show single luminosity profile while for FR IIs this percentage is 55%. Reciprocally, 56% of FR I galaxies show bulge+exponential type profiles compared to 44% of FR II galaxies.
- 2) Analysis of the photometric parameters of both FR I and FR II galaxies indicates that they have similar bulge and disk magnitudes. Moreover, both FR I and FR 2 bulges follow similar Kormendy relations. Even so, if we consider the exponential component we have that FR Is have, a) dimmer central surface magnitudes and, b) much larger scale lengths than FR IIs. K-S tests applied to the m_0 and r_0 distributions confirm these results at $> 98\%$ confidence level.

We also choose another classification scheme which relies on the spectroscopic properties, and is more likely to reflect the physical properties of the sources. We divided the sample galaxies in 4 groups, FR Is, LEGs, HEGs and QSOs. The results of the analysis were similar to those obtained with the previous classification. FR I galaxies show again for the exponential component dimmer central surface magnitudes and much larger scale lengths than the rest of the selected classes ($> 98\%$ confidence level). However, we also find that these differences are less conspicuous when FR Is are compared to LEGs.

Black hole masses were also calculated using two different methods, using the Sérsic index and the bulge total luminosity. Results show a great dispersion and black hole masses obtained through L_{bulge} are on average a factor of 3 higher than those obtained through n . This result is not surprising since we did not find a clear correlation between L_{bulge} and n . Summarizing, past results on the host galaxies of FR I and FR II sources gave confusing results on their properties and morphologies. Thanks to the HST/NICMOS data we can now probe deeply into the nuclear regions of the hosts and we can clearly distinguish the contributions from the host galaxies and the nuclear sources. We show that the host galaxies have very similar bulge properties while there seems to be a real difference in the properties or presence of disks. These results indicate that the formation histories of the different classes of radio galaxies may be significantly different.

Support for this work was provided by the National Science Foundation through grant N1183 from the Association of Universities for Research in Astronomy, Inc., under NSF cooperative agreement AST-0132798.

DM is supported by NASA LTSA NNG04GE12G.

This research has made use of the NASA Astrophysics Data System Bibliographic services. This research also made use of the NASA/IPAC Extragalactic Database (NED) which is operated by the Jet Propulsion Laboratory, California Institute of Technology, under contract with the National Aeronautics and Space Administration.

REFERENCES

- Aller, M. C., & Richstone, D. 2002, AJ 124, 3035
- Bagget, W. E., Bagget, S. M., & Anderson, K. S. J. 1998, AJ, 116, 1626
- Bennett, A. S. 1962a, Mem. RAS, 68, 163
- Bennett, A.S. 1962b, MNRAS, 125, 75

- Blandford, R.D. 2000, RSPTA, 358, 811
- Brown, R.J.N., Forbes, D.A., Silva, D., Helsdon, S.F., Ponman, T.J., Hau, G.K.T, Brodie, J.P., Goudfrooij, P, & Bothum, G. 2003, MNRAS, 341, 747
- Byum, Y. I. & Freeman, K. 1995, ApJ, 448, 563
- Chiaberge, M., Capetti, A, Celotti, A. 2002, A&A, 394, 791
- Ciotti, L. 1991, A&A, 249,99
- de Jong, R.S., Simard, L., Davies, R.L., Saglia, R.P., Burstein, D., Colless, M., McMahan, R., & Wegner, G. 2004, MNRAS, 355, 1155
- de Vaucouleurs, G. 1948, Ann. d’Astrophys., 11, 247
- Dickinson, M.E., et al. 2002, HST NICMOS data handbook v5.0, ed. B. Mobasher, Baltimore, STScI
- Djorgovski, S. & Davis, M. 1987, ApJ, 313, 59
- Dressler, A., Lynden-Bell, D., Burstein, D., Davies, R. L., Faber, S. M., Terlevich, R., & Wegner, G. 1987, ApJ, 313, 42
- Dunlop, J.S., McLure, R.J., Kukula, M.J., Baum, S.A., O’Dea, C.P., & Hughes, D.H. 2003, MNRAS, 340, 1095
- Fanaroff, B. L. & Riley, J. M. 1974, MNRAS, 167, 31
- Ferrarese, L., & Merrit, D. 2000 ApJ, 539, L9
- Freeman, K. C. 1970, ApJ, 160, 811
- Graham, A.W., Erwin, P., Caon, N., & Trujillo, I. 2003, in Galaxy Evolution: Theory and Observations, RevMexAA (SC), eds ., V. Avila-Reese, C. Firmani, C.S. Frenk, & C. Allen, Vol 17, 196-197
- Graham, A.W., & Driver, S.P. 2006 astro-ph/0607378
- Gonzalez-Serrano, J.I., Carballo, R., Perez-Fournon, I. 1993, AJ, 105, 1710
- Hardcastle, M.J., & Worrall, D.M. 2000, MNRAS, 319, 562
- Héraudeau, P., & Simien, F. 1996, A&AS, 118, 111

- Hine, R.G., & Longair, M.S. 1979, MNRAS, 118, 111
- Jackson, N., & Rawlings, S. 1997, MNRAS, 286, 241
- Jedrzejewski, R. 1987, MNRAS, 226, 747
- Kauffmann, G., & Haehnelt, M. 2000, MNRAS, 311, 576
- Krist, J. 1993, in ASP Conf. Ser. 52, *Astronomical Data Analysis Software and Systems II*, ed. R.J. Hanisch, R.J.V Brissenden, & J. Barnes (San Francisco: ASP), 536
- Koekemoer, A. M., Fruchter, A. S., Hook, R. N., & Hack, W. 2002, in *The 2002 HST Calibration Workshop: Hubble after the Installation of the ACS and the NICMOS Cooling System*, ed. S. Arribas, A. Koekemoer, & B. Whitmore, Baltimore, STScI, 339
- Kormendy, J. 1977, ApJ, 218, 333
- Kormendy, J., & Richstone, D. 1995, ARA&A, 33, 581
- Kormendy, J., & Kennicutt, R. C. Jr. 2004, ARA&A, 42, 603
- Laing R. A., Riley J. M., & Longair M. S. 1983, MNRAS, 204, 151
- Laning, R.A. 1994, ASPC, 54, 227
- Madrid, J. P., et al. 2006, ApJS, 164, 307 (M2006)
- Magorrian, J. et al. 1998, AJ, 115, 2285
- Marchesini, D., Capetti, A., & Celotti, A., 2005, A&A 433, 841
- Marconi, A. & Hunt, L.K. 2003, ApJ, 589, L21
- Möllenhoff, C. & Heidt, J. 2001, A&A, 368, 16 (M&H2001)
- Noll, K., et al. 2004, *NICMOS Instrument Handbook, Version 7.0*, (Baltimore: STScI)
- Pahre, M.A. 1999, ApJS, 124, 127
- Ryden, S. 1992, ApJ, 396, 445
- Sandage, A. R., Freeman, K. C., & Stokes, N. R. 1970, ApJ, 160, 831
- Sérsic, J. L. 1968, *Atlas de Galaxias Australes* (Córdoba: Obs. Astron.)

Suchkov, A. & Krist, J. 1998, Instrument Science Report NICMOS 98-018 (Baltimore: STScI)

Tully, R. B. & Fisher, J. R. 1977, A&A, 54, 661

Urry, C.M., & Padovani, P. 1995, PASP, 107, 803

Zirbel, E.L. 1996, ApJ, 473, 144 (Paper a)

Zirbel, E.L. 1996, ApJ, 473, 713 (Paper b)

Zirbel, E.L. 1997, ApJ, 476, 489

Table 1. Observation Log

Source (1)	Date (UT) (2)	α (3)	δ (4)	FR Class (5)	Morph. Class. (6)
3C17	2006 Jul 2	00 38 20.5	-02 07 41.0	II (QSO)	E pec
3C20	2005 Feb 27	00 43 09.27	+52 03 36.66	II (HEG)	—
3C28	2005 Jun 13	00 55 50.65	+26 24 36.93	II (LEG)	E
3C31	2005 Jun 17	01 07 24.99	+32 24 45.02	I	BCG; SA0-
3C33.1	2004 Aug 15	01 09 44.27	+73 11 57.2	II (QSO)	—
3C35	2005 Mar 16	01 12 02.29	+49 28 35.33	II (LEG)	—
3C52	2005 Mar 11	01 48 28.90	+53 32 27.9	II (LEG)	—
3C61.1	2004 Aug 9	02 22 36.00	+86 19 08.0	II (LEG)	—
3C66B	2004 Nov 5	02 23 11.46	+42 59 31.34	I	E
3C75N	2004 Nov 11	02 57 41.55	+06 01 36.58	I	E0
3C76.1	2005 Feb 6	03 03 15.0	+16 26 19.85	I	E1?
3C79	2004 Oct 30	03 10 00.1	+17 05 58.91	II (QSO)	E
3C83.1	2005 Mar 12	03 18 15.8	+41 51 28.0	I	E+
3C84	1998 Mar 16	03 19 48	+41 30 42	I	cD pec
3C88	2004 Nov 6	03 27 54.17	+02 33 41.82	II (LEG)	E pec?
3C98	2005 Nov 25	03 58 54.4	+10 26 03	II (HEG)	E1?
3C105	2004 Oct 26	04 07 16.46	+03 42 25.68	II (HEG)	E
3C111	2004 Dec 8	04 18 21.05	+38 01 35.77	II (QSO)	N
3C123	2004 Dec 7	04 37 04.4	+29 40 13.2	II (LEG)	—
3C129	2004 Dec 8	04 49 09.07	+45 00 39.0	I	E
3C129.1	2004 Nov 22	04 50 06.7	+45 03 06.0	I	E
3C132	2005 Nov 24	04 56 43.0	+22 49 22	II (LEG)	—
3C133	2004 Dec 13	05 02 58.4	+25 16 28.0	II (LEG)	—
3C135	2005 Apr 8	05 14 08.3	+00 56 32.0	II (HEG)	E
3C153	2005 Nov 25	06 09 32.5	+48 04 15	II (LEG)	—
3C165	2005 Apr 26	06 43 06.6	+23 19 03.0	II (LEG)	—
3C166	2005 Nov 4	06 45 24.1	+21 21 51	II (LEG)	E
3C171	2004 Nov 14	06 55 14.72	+54 08 58.27	II (HEG)	N
3C173.1	2004 Nov 22	07 09 24.34	+74 49 15.19	II (LEG)	—
3C180	2005 Feb 20	07 27 04.77	-02 04 30.97	II (LEG)	—
3C184.1	2004 Nov 26	07 43 01.28	+80 26 26.3	II (QSO)	E
3C192	2005 Jan 8	08 05 35.0	+24 09 50.0	II (HEG)	—
3C196.1	2005 Feb 1	08 15 27.73	-03 08 26.99	II (QSO)	cD
3C197.1	2005 Apr 19	08 21 33.7	+47 02 37.0	II (HEG)	—
3C198	2005 May 3	08 22 31.9	+05 57 7.0	II (HEG)	E
3C213.1	2005 Feb 12	09 01 05.3	+29 01 46.0	II (LEG)	—
3C219	2004 Sep 14	09 21 8.64	+45 38 56.49	II (QSO)	—
3C223	2005 Feb 10	09 39 52.76	+35 53 59.12	II (QSO)	E2
3C223.1	2005 Jan 18	09 41 24.04	+39 44 42.39	II (HEG)	S0?
3C227	2005 Mar 28	09 47 45.14	+07 25 20.33	II (QSO)	N
3C234	2005 Nov 3	10 01 49.5	+28 47 09	II (QSO)	N
3C236	2004 Nov 2	10 06 01.7	+34 54 10.0	II (LEG)	E
3C264	1998 May 12	11 45 05.0	+19 36 23	I	E
3C277.3	2005 Mar 24	12 54 12.06	+27 37 32.66	II	E
3C284	2006 Mar 4	13 11 04.7	+27 28 08	II (HEG)	—

Table 1—Continued

Source (1)	Date (UT) (2)	α (3)	δ (4)	FR Class (5)	Morph. Class. (6)
3C285	2004 Dec 5	13 21 17.8	+42 35 15.0	II (HEG)	—
3C287.1	2005 Jul 16	13 32 53.27	+02 00 44.73	II (QSO)	E pec
3C288	2004 Oct 31	13 38 50.0	+38 51 10.7	I	—
3C293	2004 Mar 17	13 52 17.8	+31 26 46	II (LEG)	—
3C296	2006 Apr 21	14 16 52.9	+10 48 26	I	—
3C300	2006 Mar 4	14 23 01.0	+19 35 17	II (HEG)	E
3C303	2004 Dec 26	14 43 02.74	+52 01 37.5	II (QSO)	N
3C305	1998 Jul 19	14 49 21.6	+63 16 14	I	SB0
3C310	2004 Aug 13	15 04 57.18	+26 00 56.87	I	—
3C314.1	2005 Feb 24	15 10 23.12	+70 45 53.4	I	E
3C315	2004 Dec 30	15 13 40.0	+26 07 27.0	I	—
3C317	1998 Aug 26	15 16 44.5	+07 01 17	I	cD; E
3C319	2004 Dec 29	15 24 05.5	+54 28 14.6	II (LEG)	—
3C326	2006 Apr 21	15 52 09.1	+20 05 24	II (LEG)	—
3C332	2006 Jan 12	16 17 42.5	+32 22 35	II (QSO)	E
3C338	1997 Dec 17	16 28 38.5	+39 33 06	I	—
3C346	2005 May 19	16 43 48.69	+17 15 48.09	II (LEG)	E
3C348	2005 May 9	16 51 08.16	+04 59 33.84	I	E
3C349	2005 Mar 23	16 59 28.84	+47 02 56.8	II (HEG)	—
3C353	2004 Sep 9	17 20 28.16	-00 58 47.06	II (LEG)	SA0-
3C357	2006 Mar 25	17 28 18.5	+31 46 14	II (HEG)	E
3C379.1	2004 Nov 5	18 24 32.53	+74 20 58.64	II (HEG)	—
3C381	2004 Nov 11	18 33 46.29	+47 27 02.9	II (HEG)	—
3C386	2005 Jun 15	18 38 26.27	+17 11 49.57	I	SA0-
3C388	2004 Oct 19	18 44 02.4	+45 33 30.0	II (LEG)	—
3C401	2004 Aug 11	19 40 25.14	+60 41 36.85	II (LEG)	E
3C402	2004 Dec 10	19 41 46.0	+50 35 44.9	II (HEG)	S?
3C403	2004 Nov 6	19 52 15.81	+02 30 24.4	II (HEG)	S0
3C405	1997 Dec 16	19 59 28.3	+40 44 02	II (HEG)	S?
3C424	2006 Jun 22	20 48 12.0	+07 01 17.0	I	E
3C433	2004 Aug 18	21 23 44.6	+25 04 28.5	II (HEG)	—
3C436	2004 Nov 9	21 44 11.74	+28 10 18.67	II (HEG)	—
3C438	2004 Nov 18	21 55 52.3	+38 00 30.0	II (HEG)	—
3C449	2004 Nov 11	22 31 20.63	+39 21 30.07	I	—
3C452	2004 Nov 28	22 45 48.9	+39 41 14.47	II (HEG)	E
3C459	2006 Jun 24	23 16 35.2	+04 05 18.0	II (LEG)	N
3C465	2004 Sep 28	23 38 29.41	+27 01 53.03	I	cD; E+ pec

Note. — Col. (1), 3CR number; col. (2) HST observation date; col. (3) right ascension for epoch 2000; col. (4) declination for epoch 2000; col. (5) FR class; col. (6) morphological classification.

Table 2. Photometrical Properties of the NICMOS Snapshot Survey

Source (1)	ellip. (2)	z (3)	m_e (4)	r_e (5)	n (6)	m_0 (7)	r_0 (8)	M_{bulge} (9)	M_{disk} (10)	M_{total} (11)	b/d (12)
3C17	0.25	0.21968	18.28	3.21	0.370	—	—	-24.88	—	-24.88	—
3C20	0.05	0.17400	17.89	2.33	0.350	—	—	-24.43	—	-24.43	—
3C28	0.18	0.19520	17.76	1.05	0.821	17.25	4.49	-22.49	-25.36	-25.43	0.07
3C31	0.11	0.01670	18.09	5.22	0.272	—	—	-25.50	—	-25.50	—
3C33.1	0.09	0.18090	18.65	3.08	0.443	—	—	-24.16	—	-24.16	—
3C35	0.27	0.06700	18.77	5.89	0.371	—	—	-25.13	—	-25.13	—
3C52	0.31	0.28540	19.06	8.34	0.240	—	—	-26.63	—	-26.63	—
3C61.1	0.07	0.18400	19.52	2.86	0.282	—	—	-23.40	—	-23.40	—
3C66.B	0.15	0.02150	19.31	9.16	0.248	19.94	20.69	-25.58	-25.32	-26.21	1.27
3C75.N	0.03	0.02315	17.10	1.98	0.247	—	—	-24.41	—	-24.41	—
3C76.1	0.15	0.03240	16.70	1.08	0.261	19.15	5.19	-23.45	-23.05	-24.02	1.46
3C79	0.10	0.25595	18.38	4.27	0.348	—	—	-25.56	—	-25.56	—
3C83.1	0.25	0.02550	18.93	12.01	0.214	—	—	-26.63	—	-26.63	—
3C84	0.22	0.01756	18.73	6.52	0.356	18.22	8.12	-25.33	-25.11	-25.98	1.23
3C88	0.35	0.03022	19.18	4.92	0.227	18.11	6.57	-24.42	-24.68	-25.31	0.79
3C98	0.15	0.03000	18.31	3.12	0.248	—	—	-24.28	—	-24.28	—
3C105	0.28	0.08900	17.16	1.19	0.315	17.55	2.20	-23.45	-23.12	-24.05	1.35
3C111	0.25	0.04850	18.87	3.44	0.173	—	—	-24.16	—	-24.16	—
3C123	0.12	0.21770	22.28	28.65	0.166	—	—	-26.04	—	-26.04	—
3C129	0.13	0.02080	17.39	1.75	0.637	17.71	4.22	-23.33	-24.01	-24.47	0.54
3C129.1	0.24	0.02220	17.32	1.76	0.900	17.76	5.97	-23.32	-24.78	-25.03	0.26
3C132	0.18	0.21400	18.66	5.36	0.362	—	—	-25.60	—	-25.60	—
3C133	0.06	0.27750	19.44	4.74	0.319	—	—	-24.82	—	-24.82	—
3C135	0.19	0.12530	17.12	1.19	0.223	17.42	2.49	-23.78	-23.64	-24.47	1.14
3C153	0.11	0.27700	16.79	1.28	0.259	18.44	5.27	-24.75	-24.81	-25.53	0.95
3C165	0.18	0.29570	20.21	9.23	0.241	—	—	-25.72	—	-25.72	—
3C166	0.07	0.24500	21.49	14.18	0.225	—	—	-25.24	—	-25.24	—
3C171	0.08	0.23840	19.11	4.21	0.305	—	—	-24.78	—	-24.78	—
3C173.1	0.23	0.29210	19.46	9.01	0.162	—	—	-26.62	—	-26.62	—
3C180	0.43	0.22000	20.00	7.44	0.242	18.07	5.56	-25.21	-25.09	-25.91	1.11
3C184.1	0.27	0.11820	15.79	0.59	0.904	16.74	2.05	-22.87	-23.88	-24.24	0.39
3C192	0.03	0.05980	17.84	2.61	0.253	—	—	-24.39	—	-24.39	—
3C196.1	0.29	0.19800	19.03	2.41	0.337	17.75	6.65	-23.47	-25.72	-25.85	0.13
3C197.1	0.08	0.13010	19.42	4.73	0.227	—	—	-24.51	—	-24.51	—
3C198	0.15	0.08150	19.31	3.50	0.292	—	—	-23.61	—	-23.61	—
3C213.1	0.39	0.19400	18.95	4.59	0.281	—	—	-25.01	—	-25.01	—
3C219	0.23	0.17440	18.92	6.27	0.399	—	—	-25.48	—	-25.48	—
3C223	0.18	0.13680	18.71	4.06	0.286	—	—	-24.76	—	-24.76	—
3C223.1	0.45	0.10700	16.99	1.50	0.261	16.74	3.21	-24.25	-24.78	-25.30	0.61
3C227	0.17	0.08610	18.47	2.93	0.235	—	—	-24.21	—	-24.21	—
3C234	0.07	0.18500	17.88	2.78	0.433	—	—	-24.76	—	-24.76	—
3C236	0.34	0.10050	19.57	10.06	0.291	16.62	1.91	-25.72	-23.75	-25.89	6.15
3C264	0.05	0.02172	16.13	1.52	0.671	17.70	5.48	-24.37	-24.70	-25.30	0.74
3C277.3	0.05	0.08570	19.11	5.54	0.255	—	—	-24.93	—	-24.93	—
3C284	0.03	0.23900	19.44	6.13	0.213	17.59	2.00	-25.48	-23.42	-25.63	6.69

Table 2—Continued

Source (1)	ellip. (2)	z (3)	m_e (4)	r_e (5)	n (6)	m_0 (7)	r_0 (8)	M_{bulge} (9)	M_{disk} (10)	M_{total} (11)	b/d (12)
3C285	0.42	0.07940	18.63	3.00	0.239	17.87	4.89	-24.08	-24.49	-25.05	0.69
3C287.1	0.12	0.21590	16.24	1.00	0.268	18.26	4.83	-24.55	-24.58	-25.32	0.97
3C288	0.03	0.24600	18.94	4.79	0.749	18.12	7.73	-24.81	-25.83	-26.19	0.39
3C293	0.55	0.04503	17.44	1.63	0.968	17.43	4.65	-23.09	-24.66	-24.89	0.23
3C296	0.21	0.02370	17.97	6.60	0.277	—	—	-26.17	—	-26.17	—
3C300	0.29	0.27000	19.31	4.92	0.299	—	—	-24.92	—	-24.92	—
3C303	0.10	0.14100	18.93	5.30	0.259	—	—	-25.19	—	-25.19	—
3C305	0.35	0.04164	17.39	2.58	0.224	17.46	5.44	-24.88	-24.97	-25.67	0.92
3C310	0.15	0.05350	18.09	2.56	0.285	18.85	8.40	-24.06	-24.55	-25.09	0.63
3C314.1	0.41	0.11970	18.99	4.44	0.408	—	—	-24.43	—	-24.43	—
3C315	0.35	0.10830	16.83	1.39	0.252	18.84	4.59	-24.28	-23.47	-24.70	2.11
3C317	0.30	0.03446	17.83	1.63	0.434	17.24	7.63	-23.06	-25.89	-25.97	0.07
3C319	0.24	0.19200	16.40	0.78	0.353	18.61	4.05	-23.59	-23.74	-24.42	0.87
3C326	0.39	0.08900	17.13	1.38	0.269	16.90	2.07	-23.86	-23.62	-24.50	1.25
3C332	0.05	0.15150	15.94	0.88	0.254	17.82	3.10	-24.35	-23.82	-24.87	1.63
3C338	0.28	0.03035	19.03	12.86	0.474	—	—	-26.29	—	-26.29	—
3C346	0.30	0.16100	14.90	0.46	0.270	17.83	3.82	-23.98	-24.29	-24.90	0.76
3C348	0.22	0.15400	19.58	9.25	0.925	—	—	-25.16	—	-25.16	—
3C349	0.48	0.20500	17.27	1.48	0.249	17.89	3.45	-24.20	-24.02	-24.87	1.18
3C353	0.03	0.03043	17.86	1.85	0.251	18.11	3.43	-23.53	-23.24	-24.15	1.31
3C357	0.32	0.16700	18.94	5.29	0.238	17.94	5.17	-25.34	-24.87	-25.88	1.54
3C379.1	0.11	0.25600	18.14	2.77	0.225	17.83	5.02	-25.06	-25.22	-25.89	0.87
3C381	0.17	0.16050	17.10	1.56	0.264	17.78	2.86	-24.43	-23.71	-24.88	1.95
3C386	0.12	0.01700	18.32	3.38	0.226	—	—	-24.38	—	-24.38	—
3C388	0.13	0.09100	17.64	2.21	1.227	16.86	5.37	-23.62	-25.71	-25.86	0.14
3C401	0.18	0.20104	17.89	1.17	0.310	17.97	5.34	-22.95	-24.89	-25.06	0.17
3C402	0.21	0.02390	18.85	5.00	0.190	—	—	-24.76	—	-24.76	—
3C403	0.26	0.05900	18.01	4.72	0.405	—	—	-25.32	—	-25.32	—
3C405	0.25	0.05608	20.01	14.85	0.525	—	—	-25.67	—	-25.67	—
3C424	0.03	0.12699	19.38	3.67	0.254	—	—	-23.91	—	-23.91	—
3C433	0.43	0.10160	17.90	2.51	0.494	16.85	4.68	-24.08	-25.44	-25.71	0.29
3C436	0.18	0.21450	19.12	6.61	0.255	—	—	-25.75	—	-25.75	—
3C438	0.10	0.29000	19.86	9.96	0.298	—	—	-26.06	—	-26.06	—
3C449	0.48	0.01710	19.01	5.08	0.164	—	—	-24.75	—	-24.75	—
3C452	0.24	0.08110	18.15	3.83	0.276	—	—	-25.00	—	-25.00	—
3C459	0.15	0.21990	15.45	0.81	0.430	17.59	3.38	-24.63	-24.48	-25.31	1.14
3C465	0.20	0.03030	17.67	3.92	0.311	18.52	14.59	-25.25	-25.98	-26.43	0.51

Note. — Col. (1), 3CR number; col (2), ellipticity; col. (3), redshift; col. (4), effective surface magnitude; col. (5), effective radius; col. (6), Sérsic index; col. (7), central surface magnitude; col. (8), scale length; col. (9), bulge absolute magnitude; col. (10), disk absolute magnitude; col. (11), total absolute magnitude; col. (12), bulge/disk ratio.

Table 3. Average parameters for FR I and FR II galaxies

Galaxies	M_{total}	M_{bulge}	M_{disk}	m_e [mag/arcsec ²]	r_e [Kpc]	n	m_0 [mag/arcsec ²]	r_0 [Kpc]	B/D
(1)	(2)	(3)	(4)	(5)	(6)	(7)	(8)	(9)	(10)
ALL	-25.4 ± 0.7	-25.0 ± 0.9	-24.8 ± 0.6	17.6 ± 1.1	4.6 ± 2.7	0.35 ± 0.18	17.6 ± 0.7	5.3 ± 2.8	1.1 ± 1.0
FR I	-25.6 ± 0.7	-25.1 ± 0.9	-25.1 ± 0.6	17.7 ± 0.8	4.7 ± 2.6	0.40 ± 0.18	18.1 ± 0.7	8.2 ± 2.7	0.8 ± 0.4
FR II	-25.3 ± 0.6	-25.0 ± 0.7	-24.6 ± 0.6	17.5 ± 1.0	4.6 ± 2.6	0.33 ± 0.08	17.5 ± 0.4	4.0 ± 1.3	1.3 ± 0.8

Note. — Col. (1), Sub sample galaxies; (2), total absolute magnitude; Col. (3), bulge total magnitude; col. (4), disk total magnitude; col. (5), bulge effective magnitude; col. (6), bulge effective radius ; col. (7), Sérsic index; col. (8), disk central surface magnitude; col. (9), disk scale length; col. (10), bulge to disk ratio.

Table 4. Average parameters for FR I, LEG, HEG and QSO galaxies

Galaxies	M_{total}	M_{bulge}	M_{disk}	m_e [mag/arcsec ²]	r_e [Kpc]	n	m_0 [mag/arcsec ²]	r_0 [Kpc]	B/D
(1)	(2)	(3)	(4)	(5)	(6)	(7)	(8)	(9)	(10)
FR I	-25.6 ± 0.7	-25.1 ± 0.7	-25.1 ± 0.7	17.7 ± 0.9	4.7 ± 2.6	0.40 ± 0.16	18.1 ± 0.6	8.2 ± 3.1	0.8 ± 0.4
LEG	-25.5 ± 0.6	-25.2 ± 0.9	-24.7 ± 0.6	17.7 ± 1.4	5.8 ± 4.1	0.38 ± 0.10	17.5 ± 0.5	4.3 ± 1.1	1.2 ± 0.8
HEG	-25.2 ± 0.5	-24.9 ± 0.6	-24.5 ± 0.7	18.1 ± 0.8	4.2 ± 2.0	0.29 ± 0.10	17.5 ± 0.3	3.6 ± 1.1	1.6 ± 0.9
QSO	-25.0 ± 0.5	-24.7 ± 0.6	-24.8 ± 0.8	17.3 ± 0.7	3.1 ± 1.2	0.36 ± 0.11	17.5 ± 0.4	4.2 ± 1.8	0.8 ± 0.5

Note. — Col. (1), Sub sample galaxies; (2), total absolute magnitude; Col. (3), bulge total magnitude; col. (4), disk total magnitude; col. (5), bulge effective magnitude; col. (6), bulge effective radius ; col. (7), Sérsic index; col. (8), disk central surface magnitude; col. (9), disk scale length; col. (10), bulge to disk ratio.

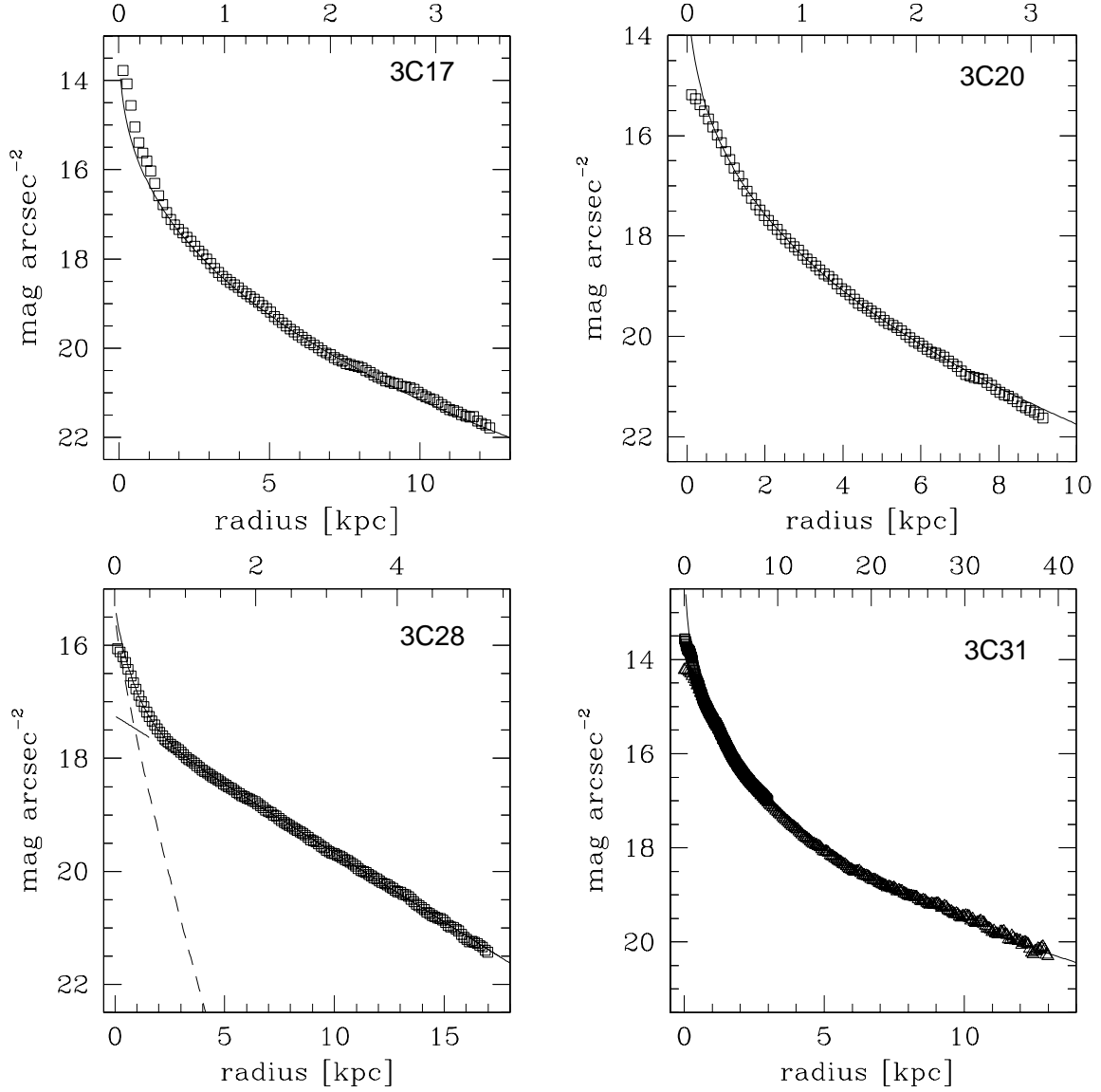


Fig. 1a.— Luminosity profiles. Squares represent NICMOS data while triangles represent TNG data. Upper ordinates give radius in units of arcsec . Solid line shows the sum of the bulge (short dashed) plus disk (long dashed) fitting functions.

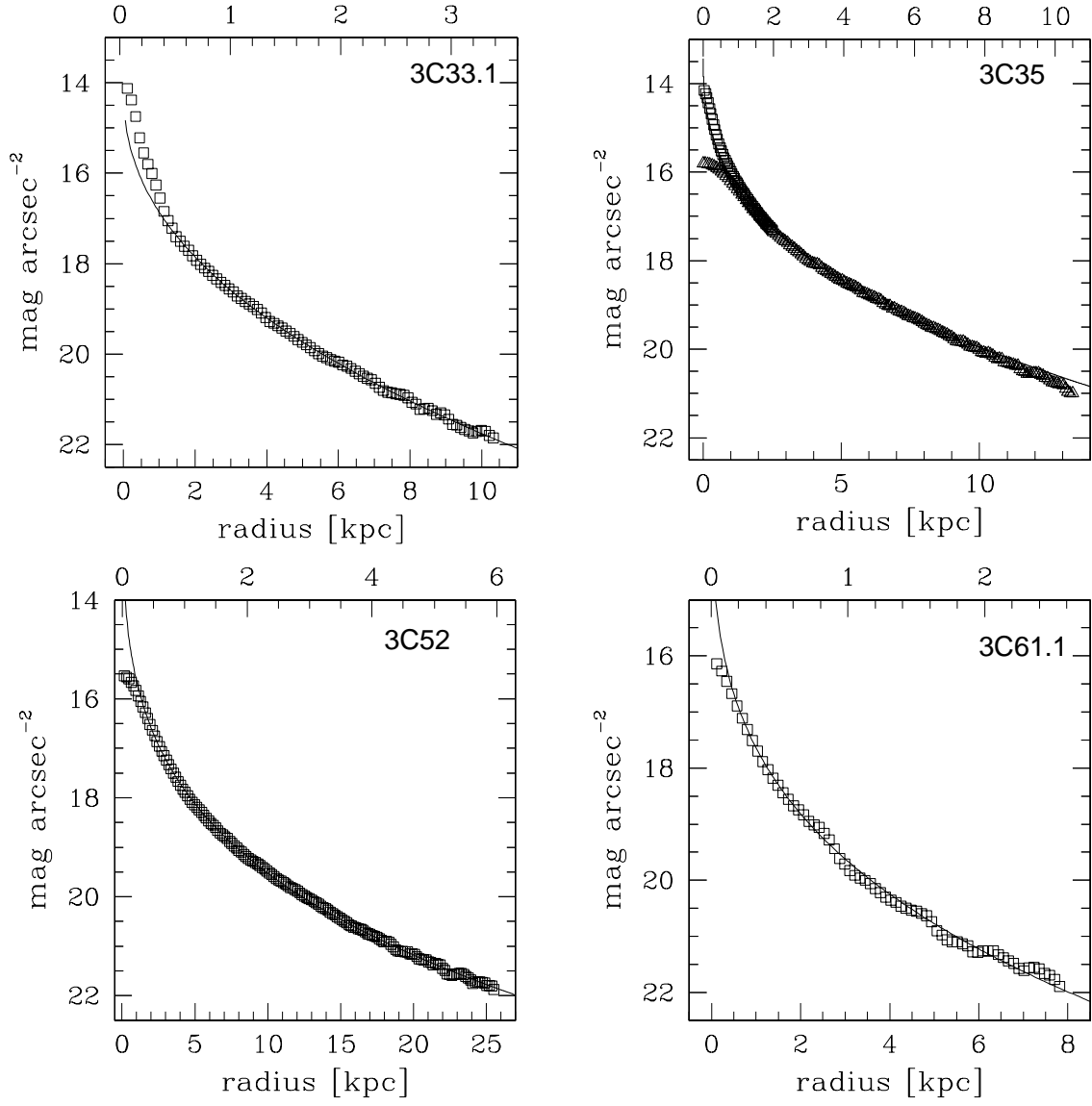


Fig. 1b.— Same as Fig. 1a.

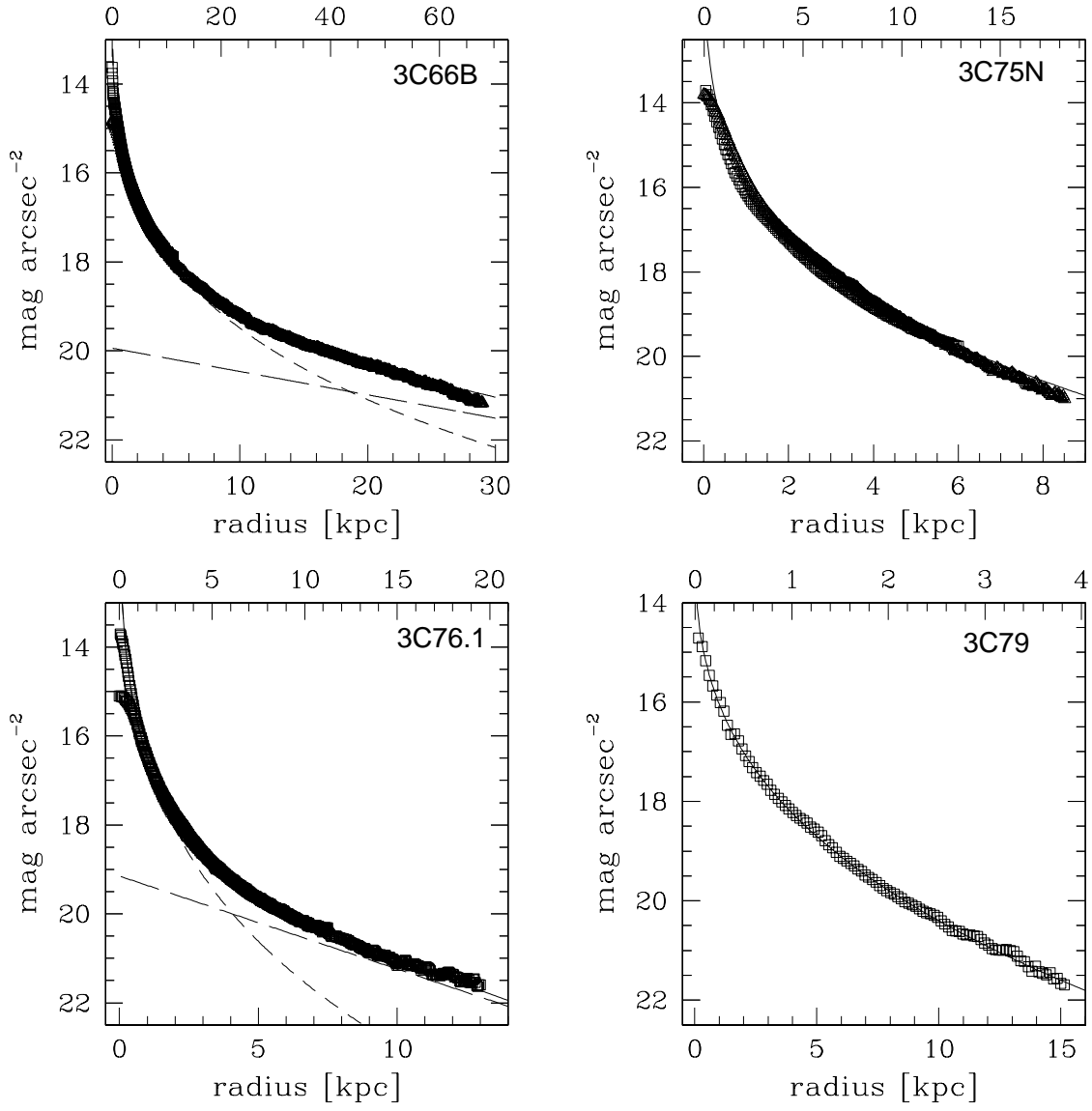


Fig. 1c.— Same as Fig. 1a.

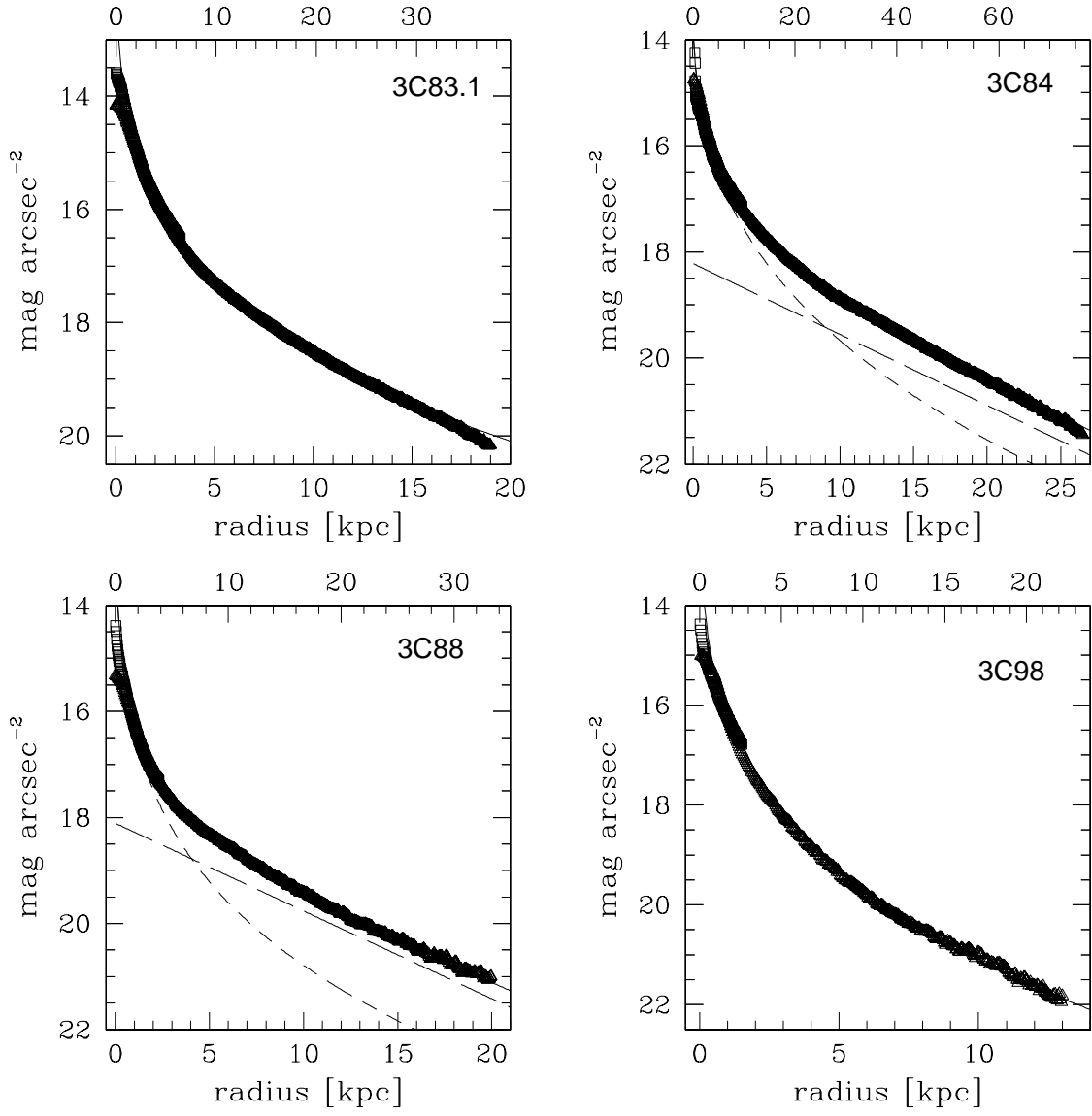


Fig. 1d.— Same as Fig. 1a.

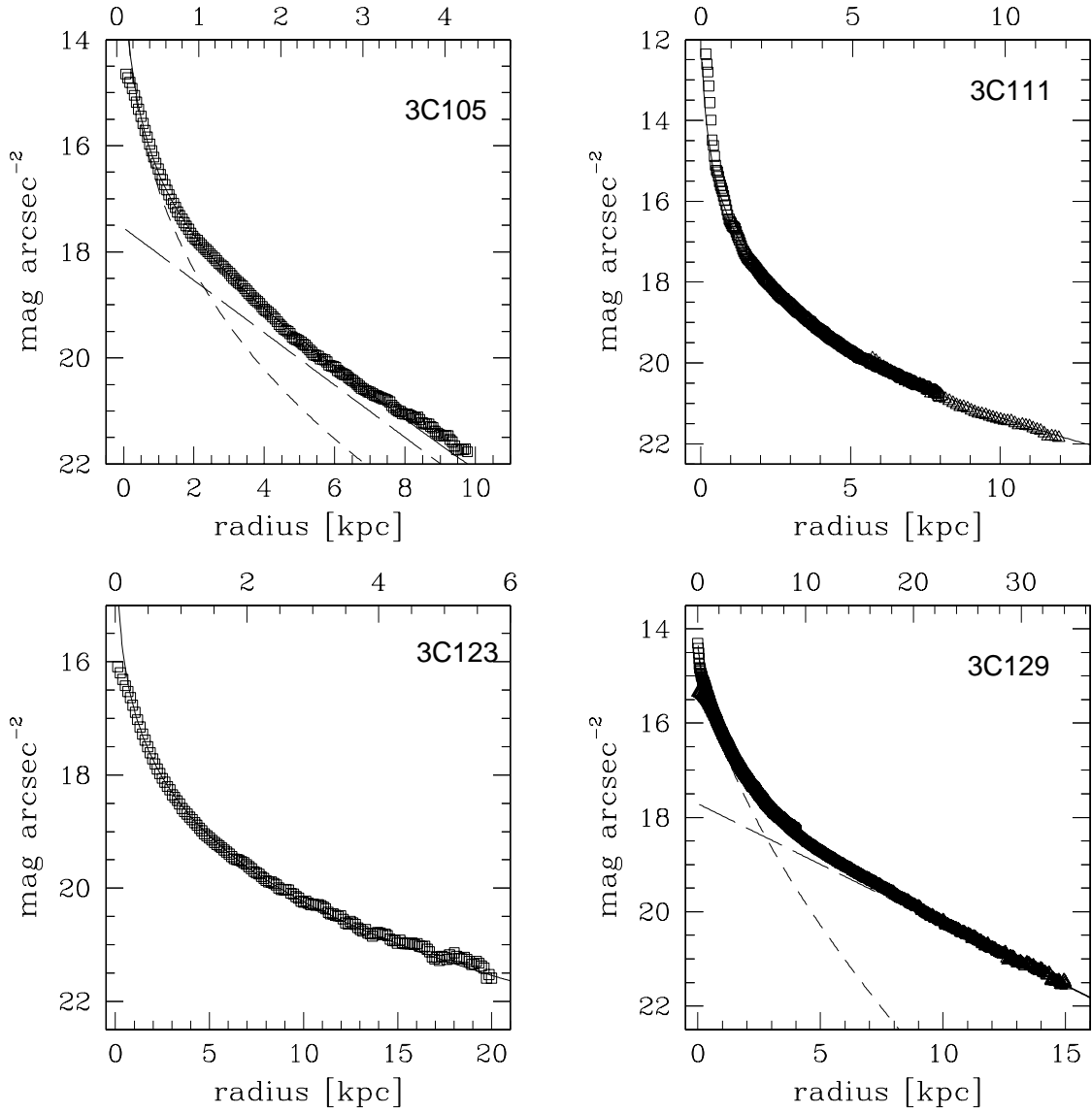


Fig. 1e.— Same as Fig. 1a.

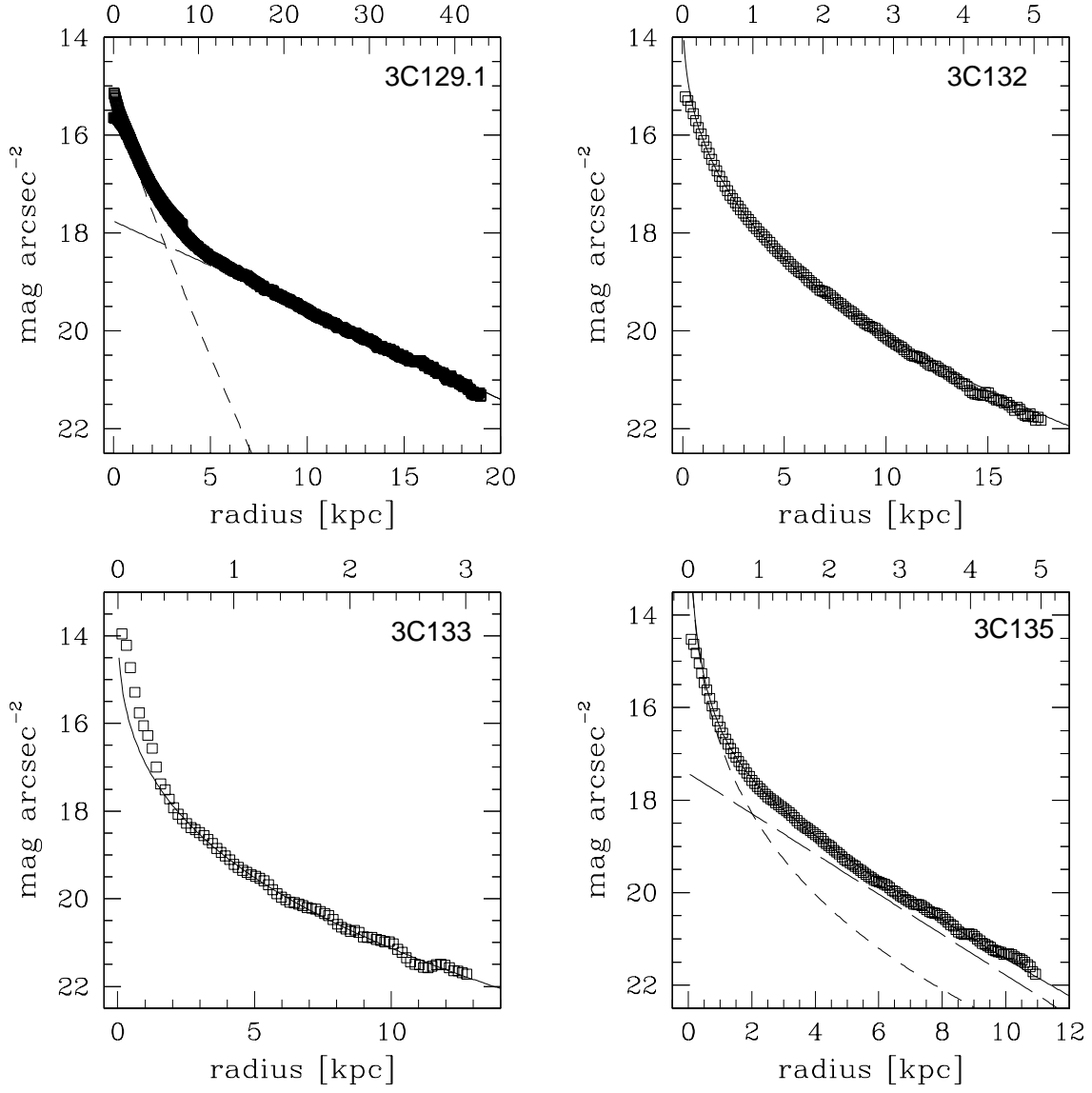


Fig. 1f.— Same as Fig. 1a.

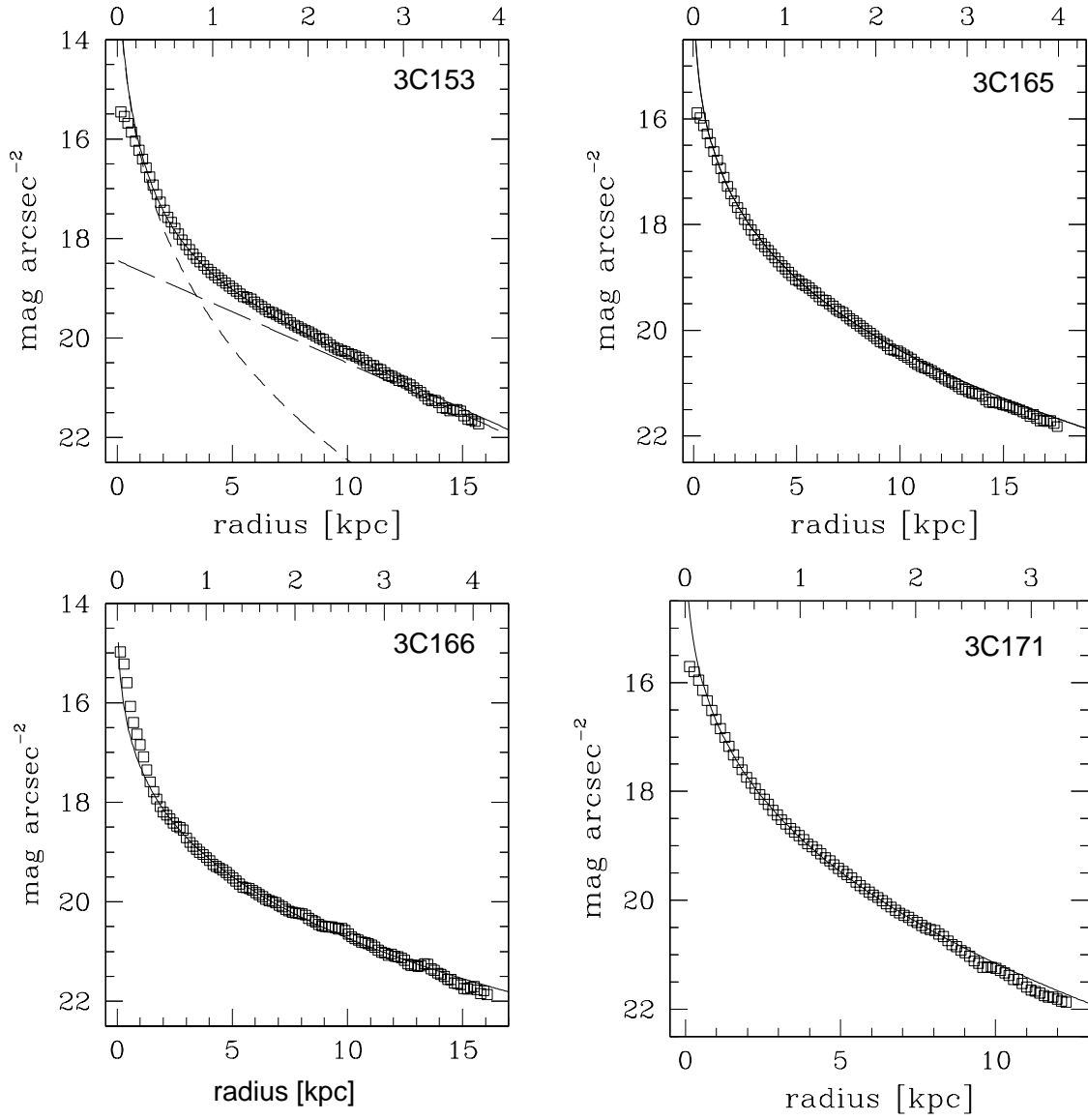


Fig. 1g.— Same as Fig. 1a.

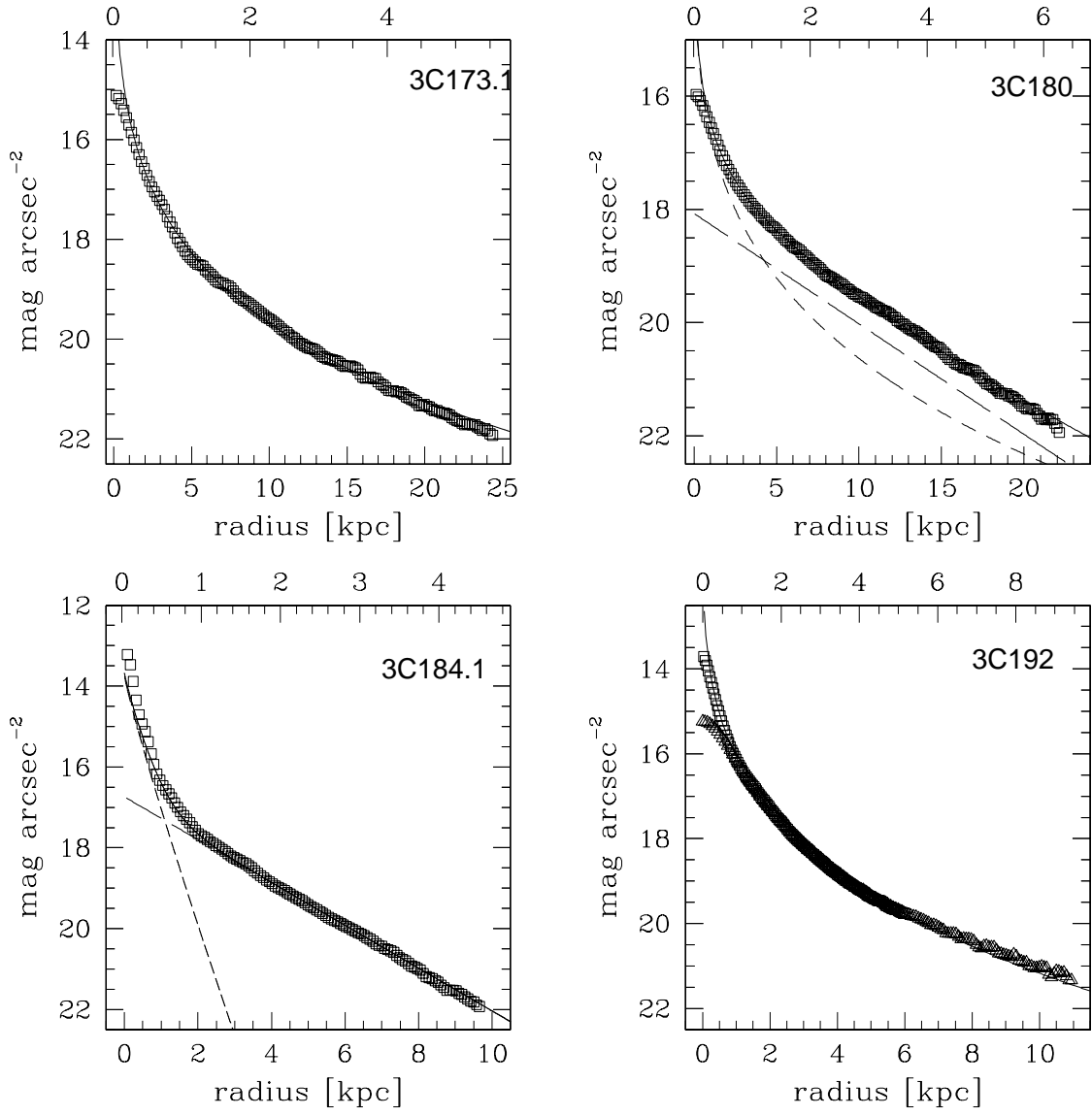


Fig. 1h.— Same as Fig. 1a.

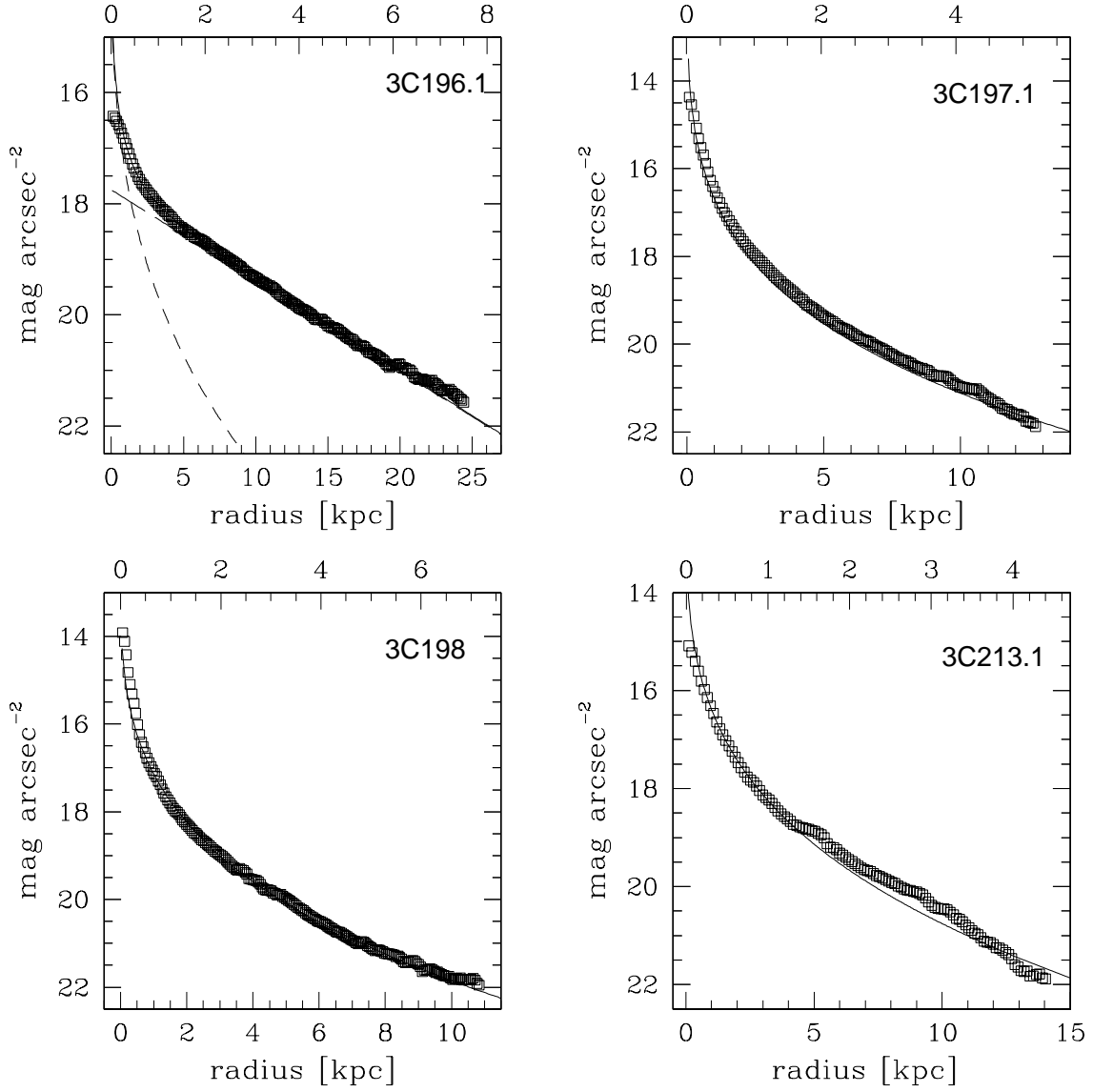


Fig. 1i.— Same as Fig. 1a.

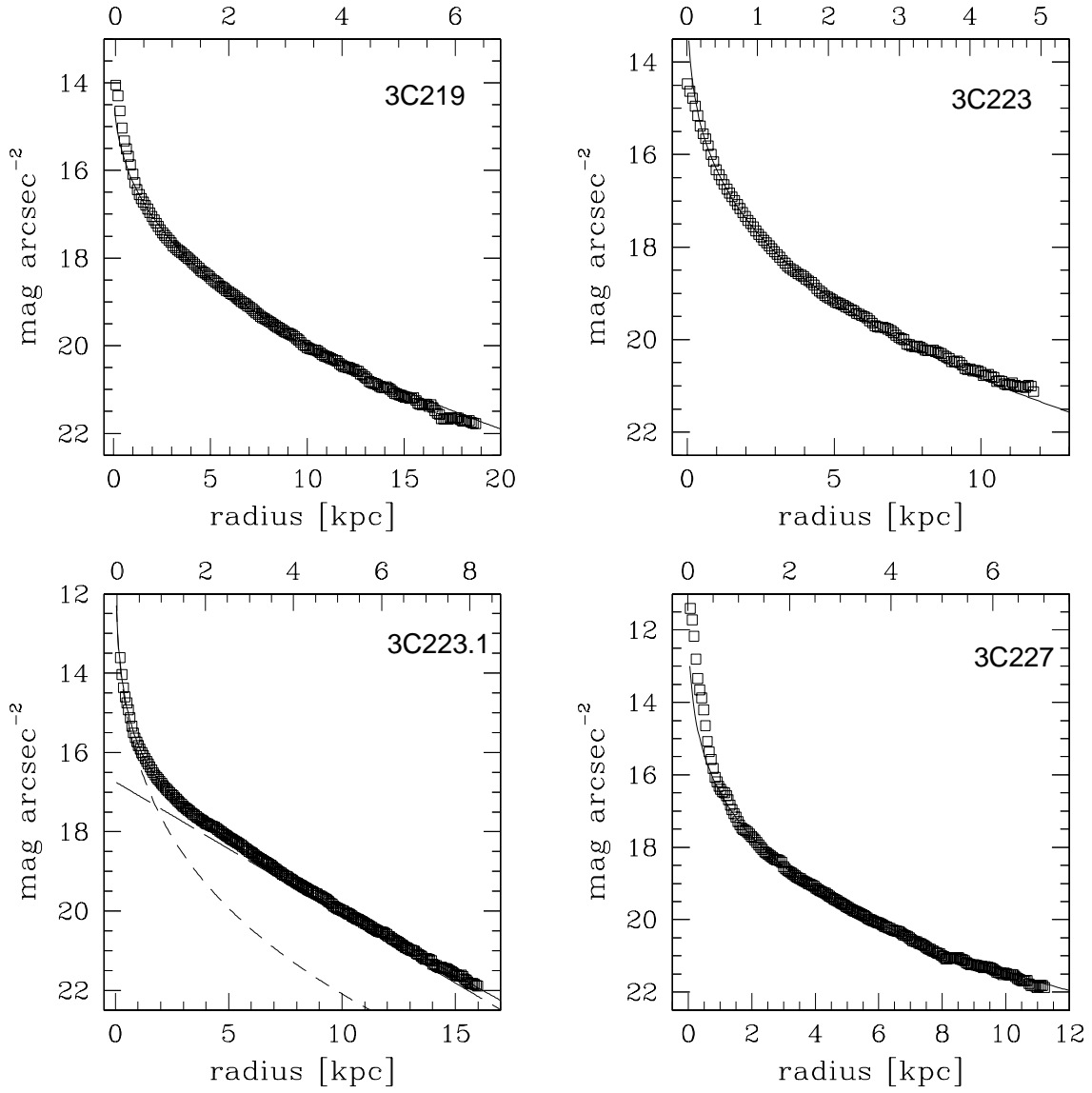


Fig. 1j.— Same as Fig. 1a.

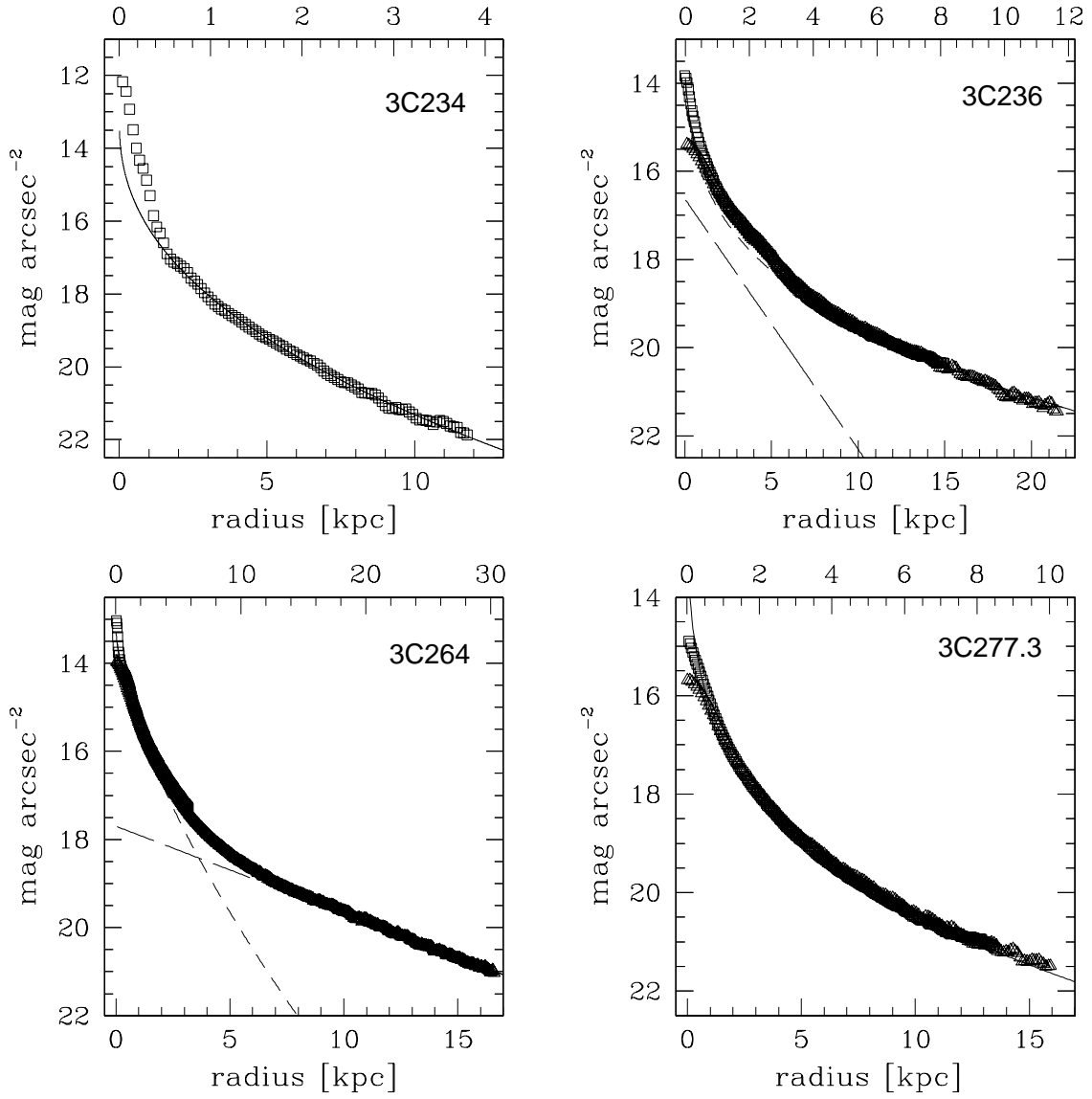


Fig. 1k.— Same as Fig. 1a.

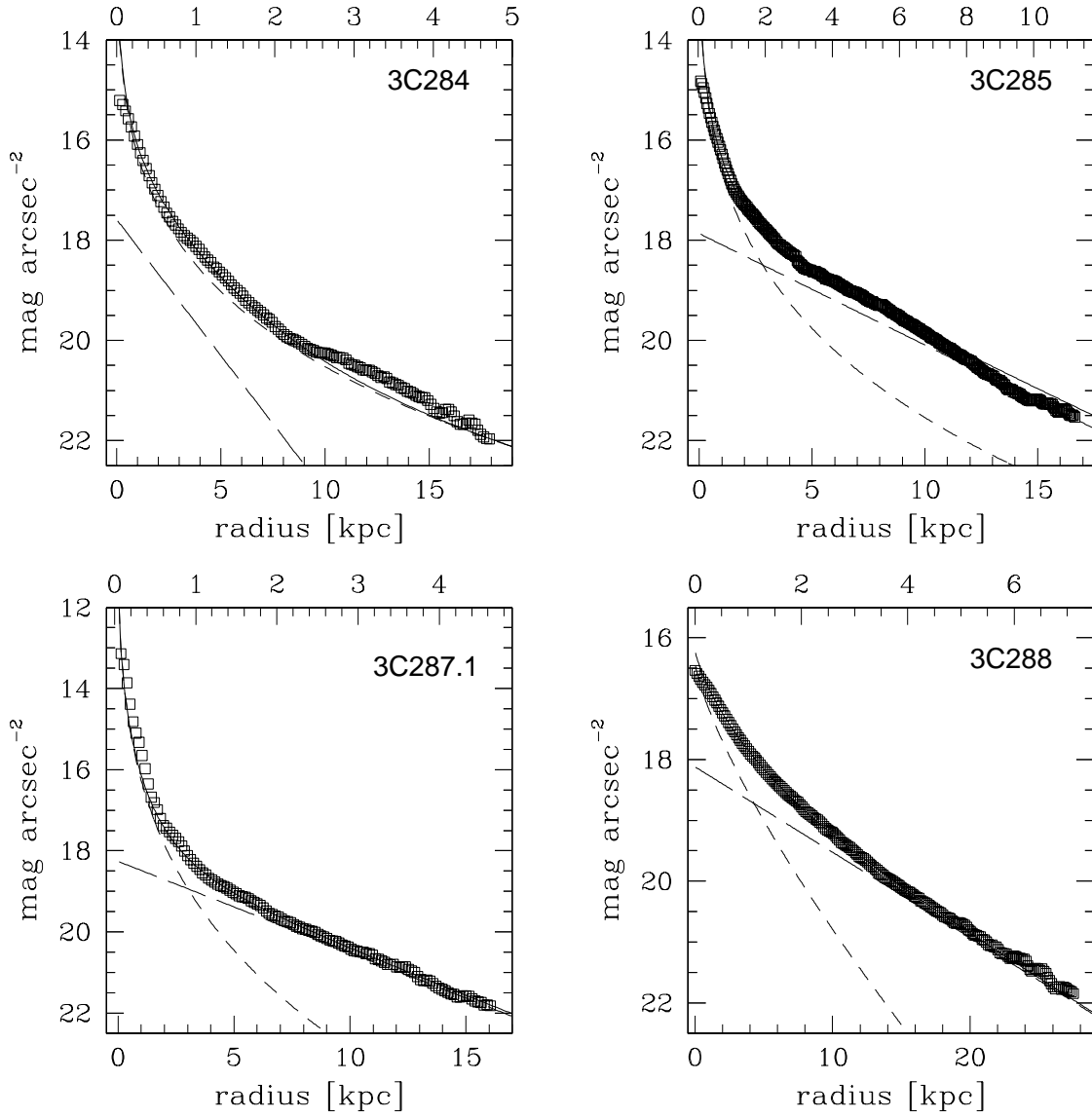


Fig. 11.— Same as Fig. 1a.

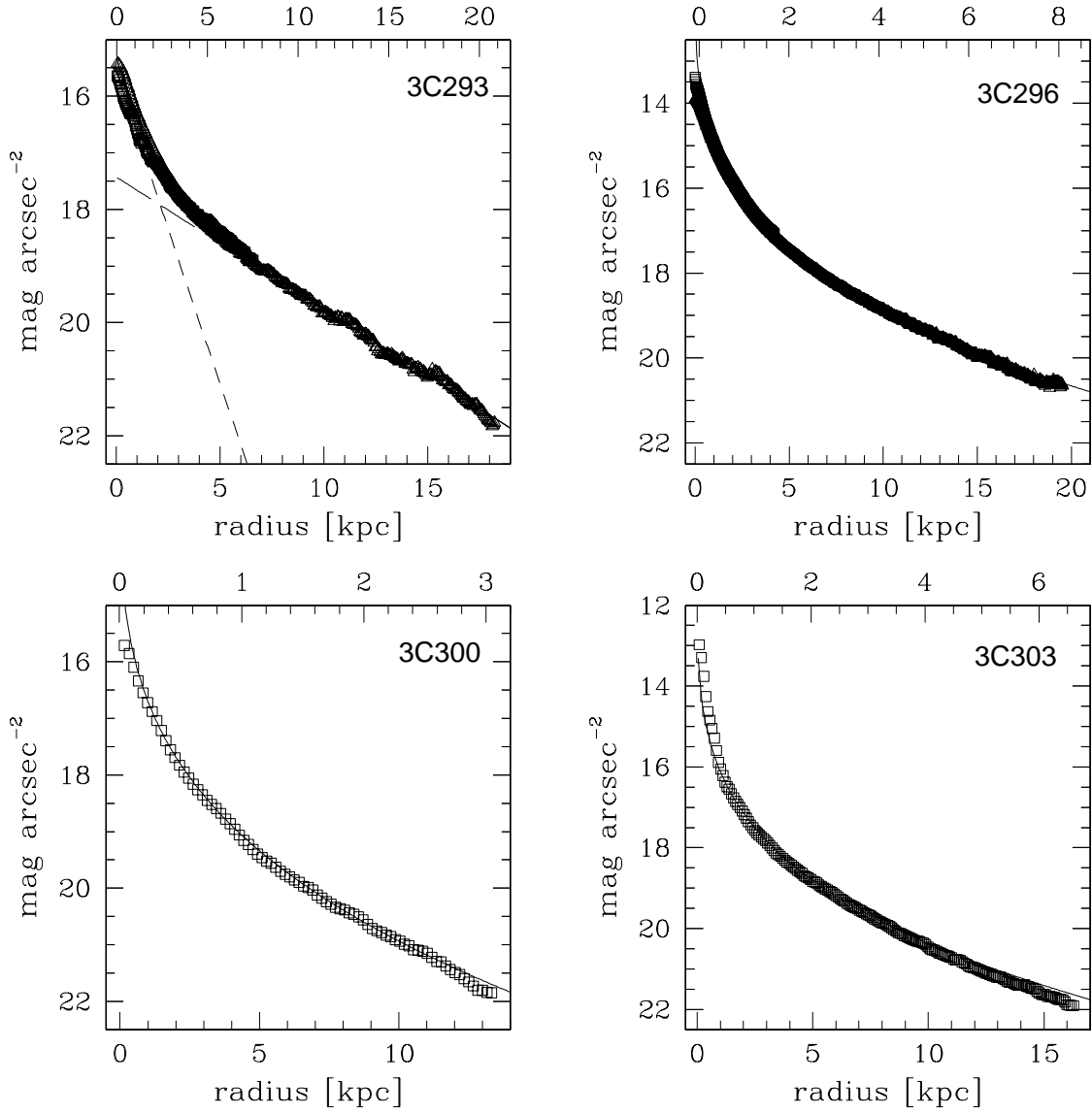


Fig. 1m.— Same as Fig. 1a.

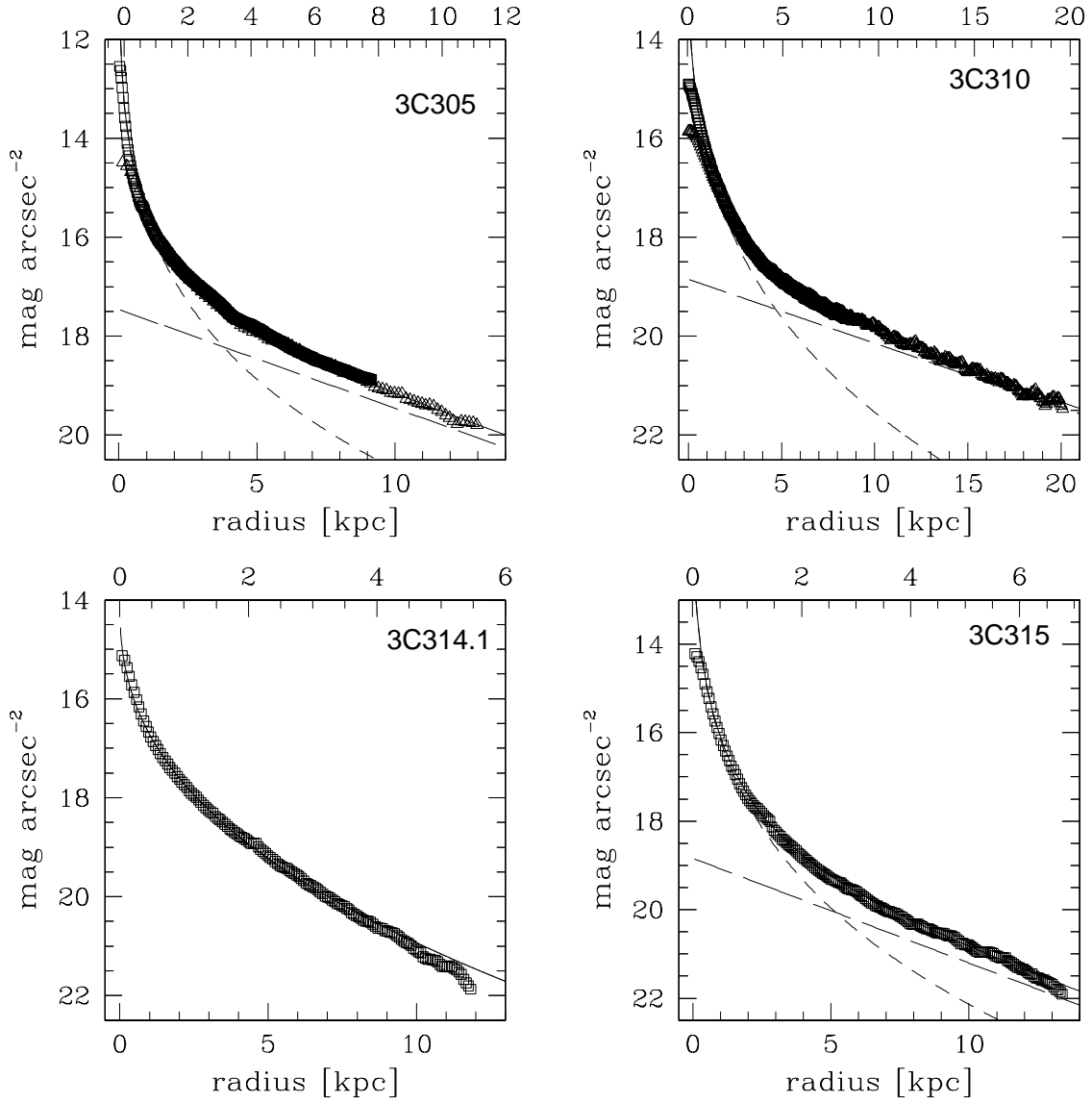


Fig. 1n.— Same as Fig. 1a.

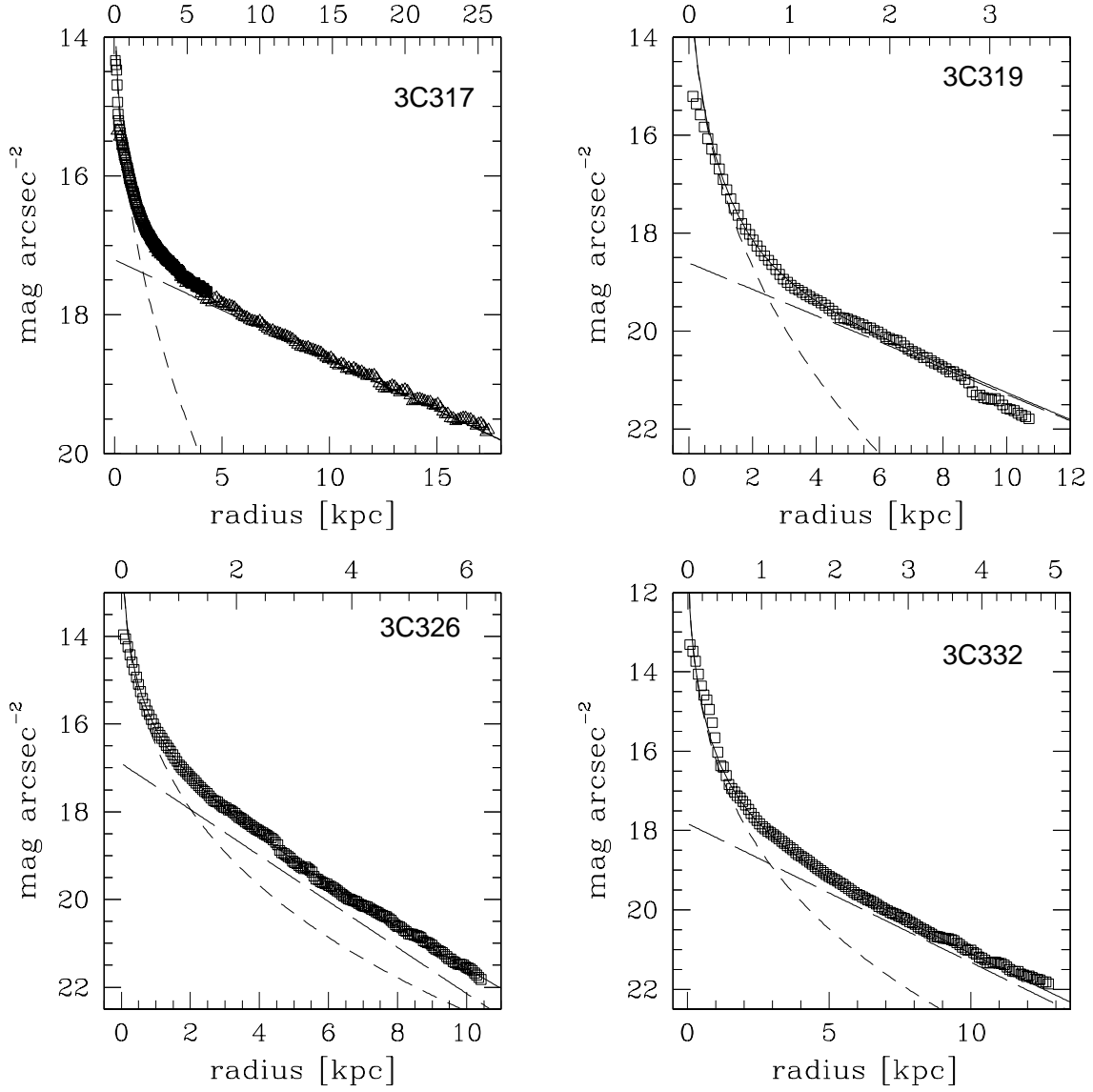


Fig. 1o.— Same as Fig. 1a.

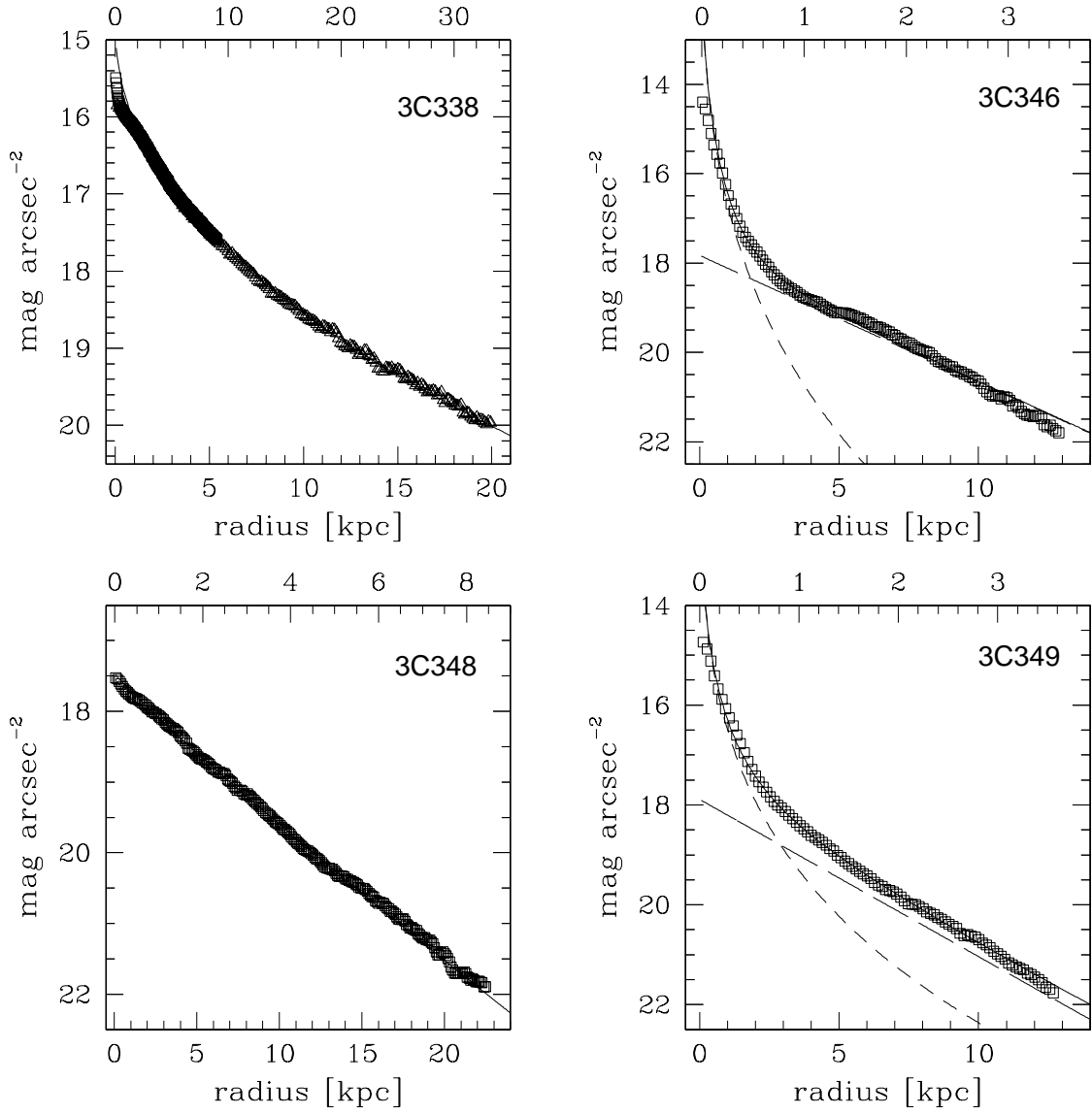


Fig. 1p.— Same as Fig. 1a.

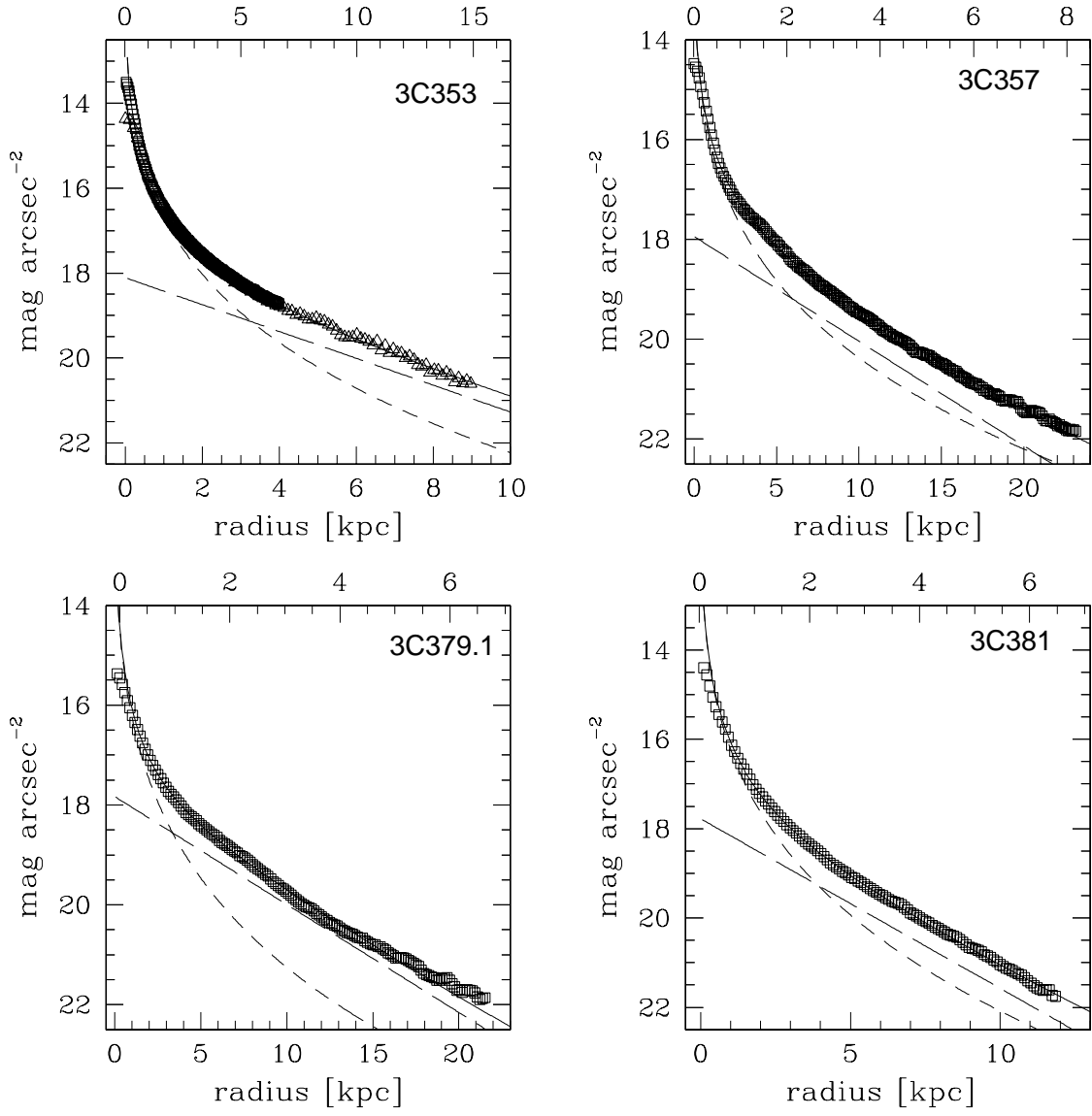


Fig. 1q.— Same as Fig. 1a.

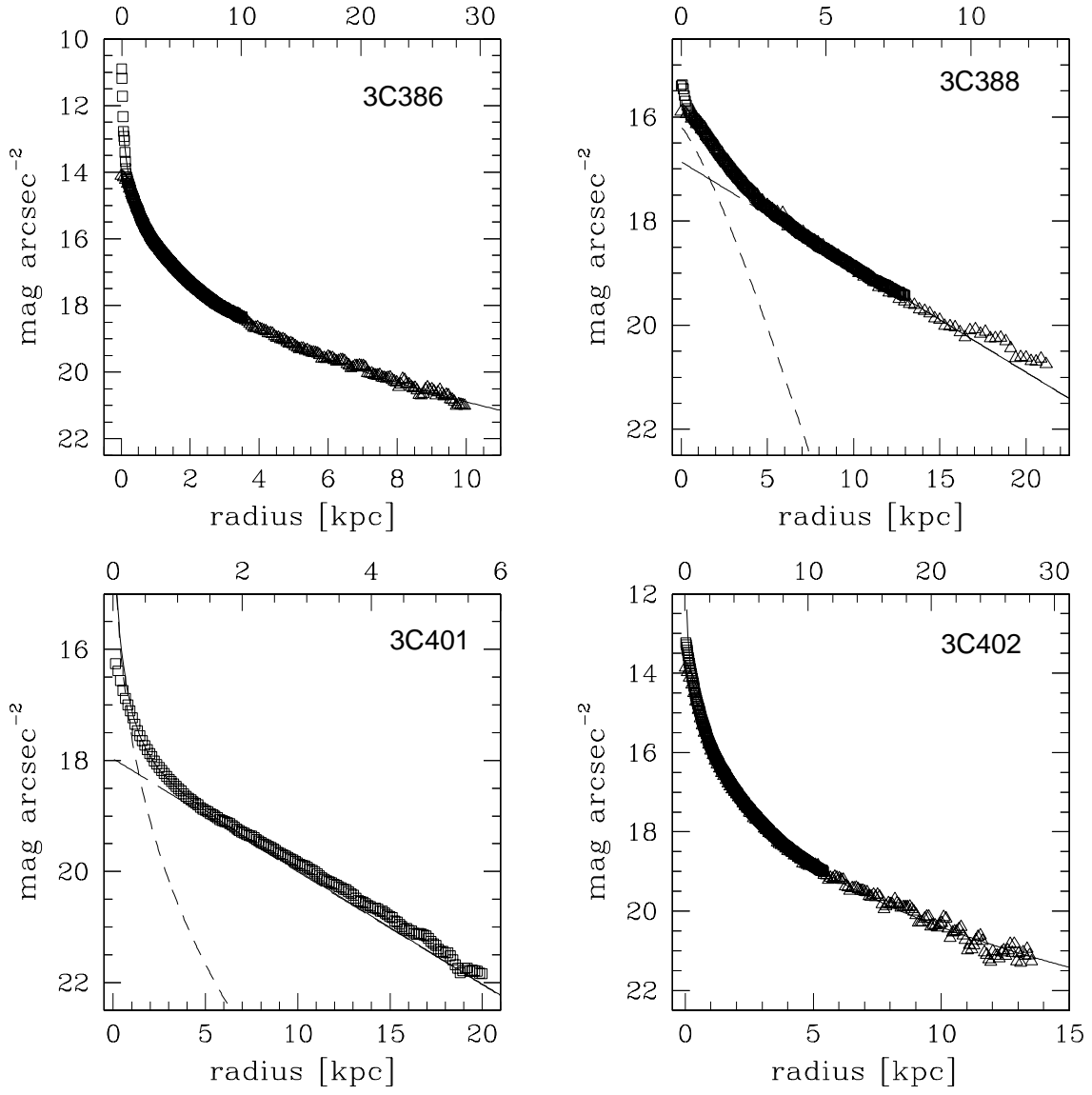


Fig. 1r.— Same as Fig. 1a.

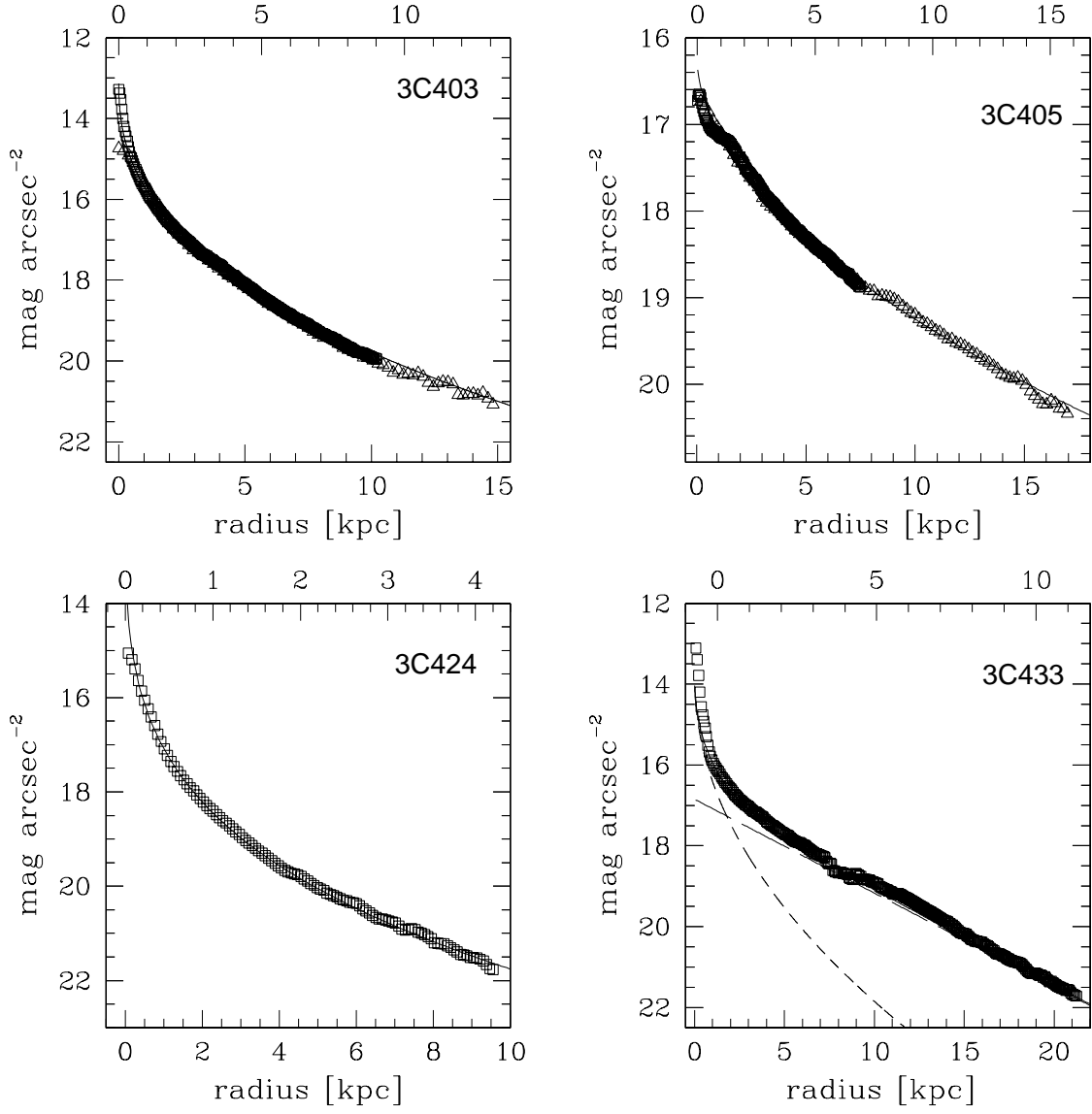


Fig. 1s.— Same as Fig. 1a.

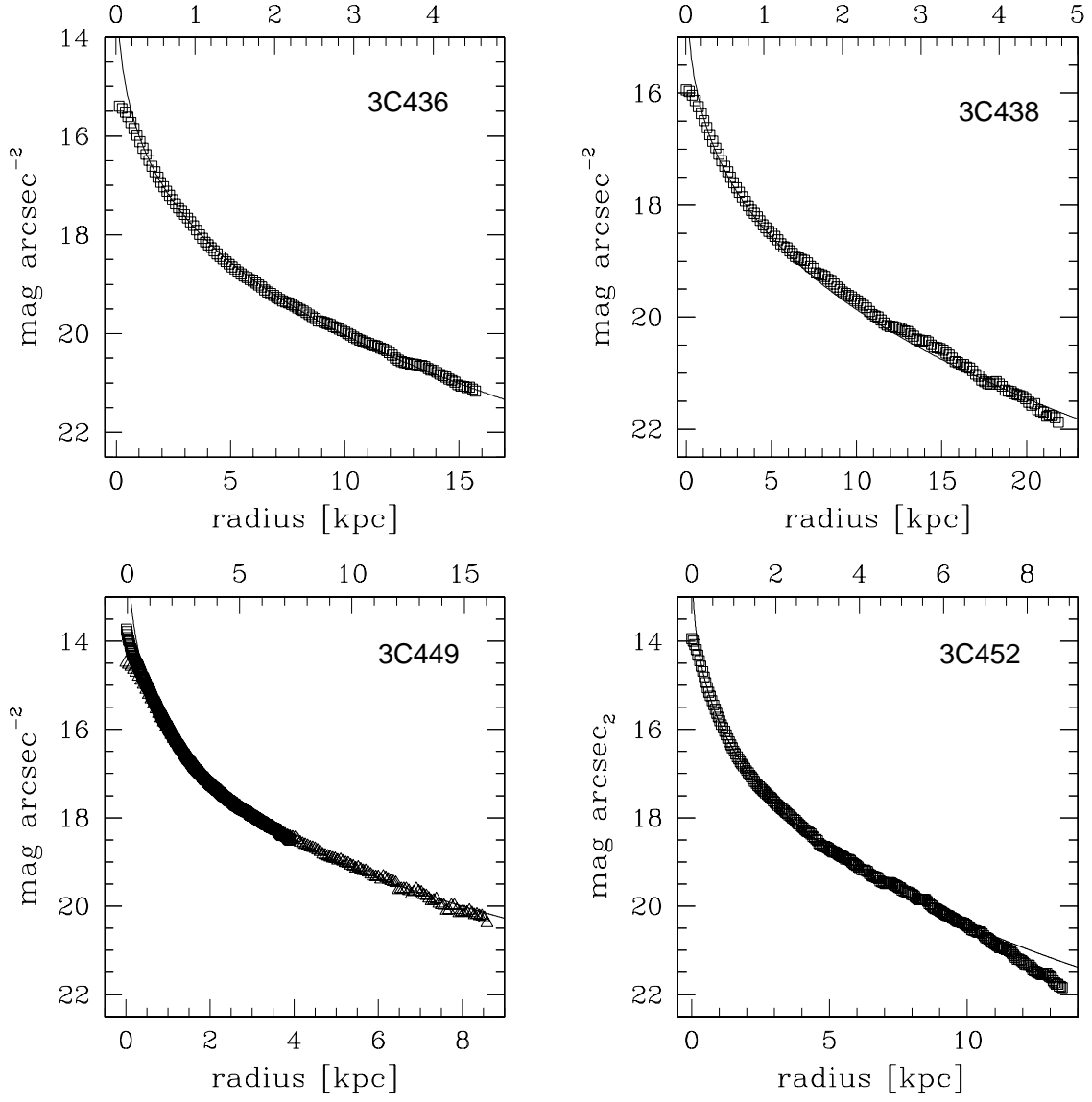


Fig. 1t.— Same as Fig. 1a.

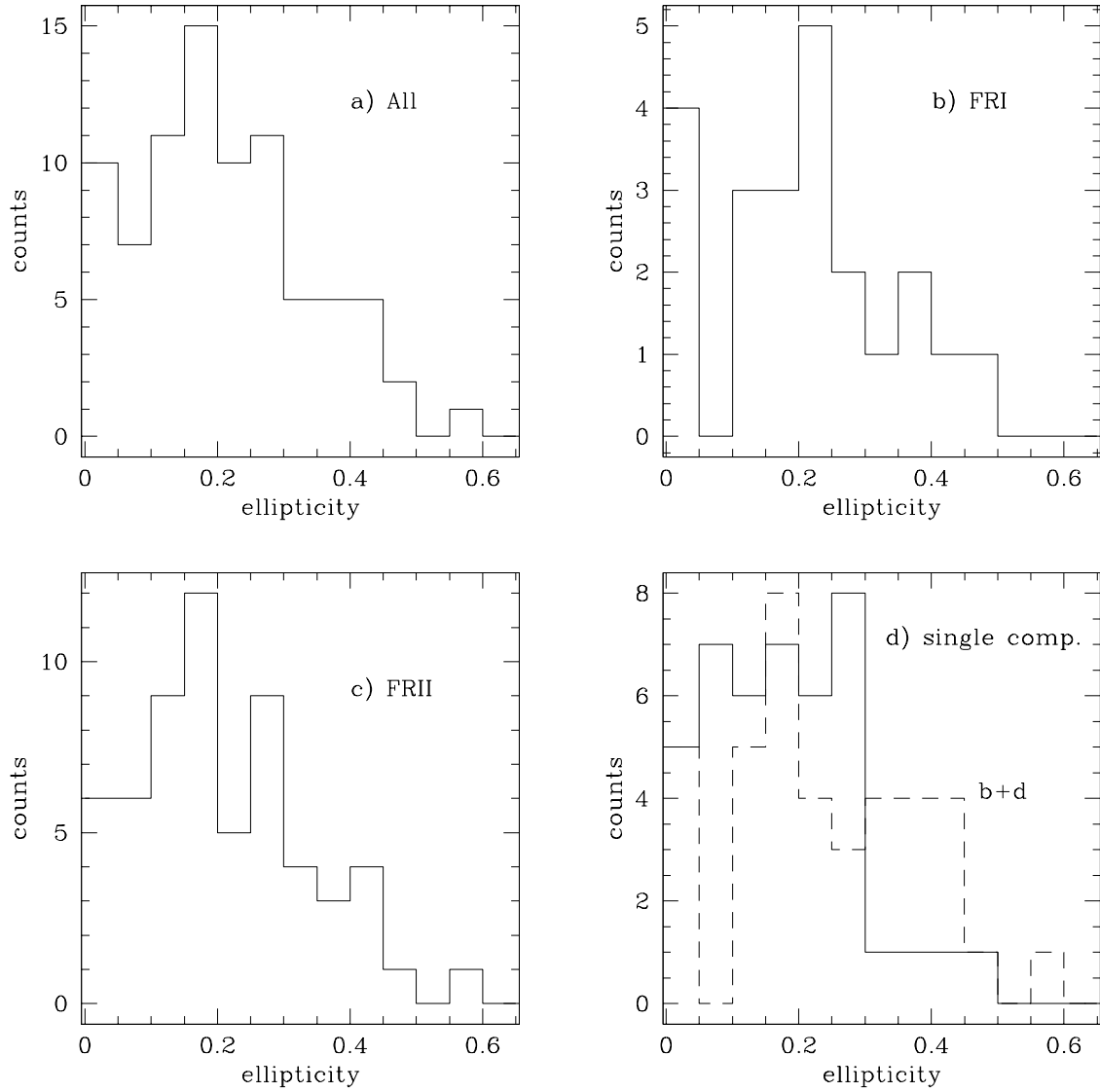


Fig. 2.— Ellipticity distributions for: a) Whole sample, b) FR I galaxies, c) FR II galaxies, d) Galaxies with single Sérsic luminosity profile (solid line histogram) and for bulge+disk luminosity profile galaxies (dashed line histogram).

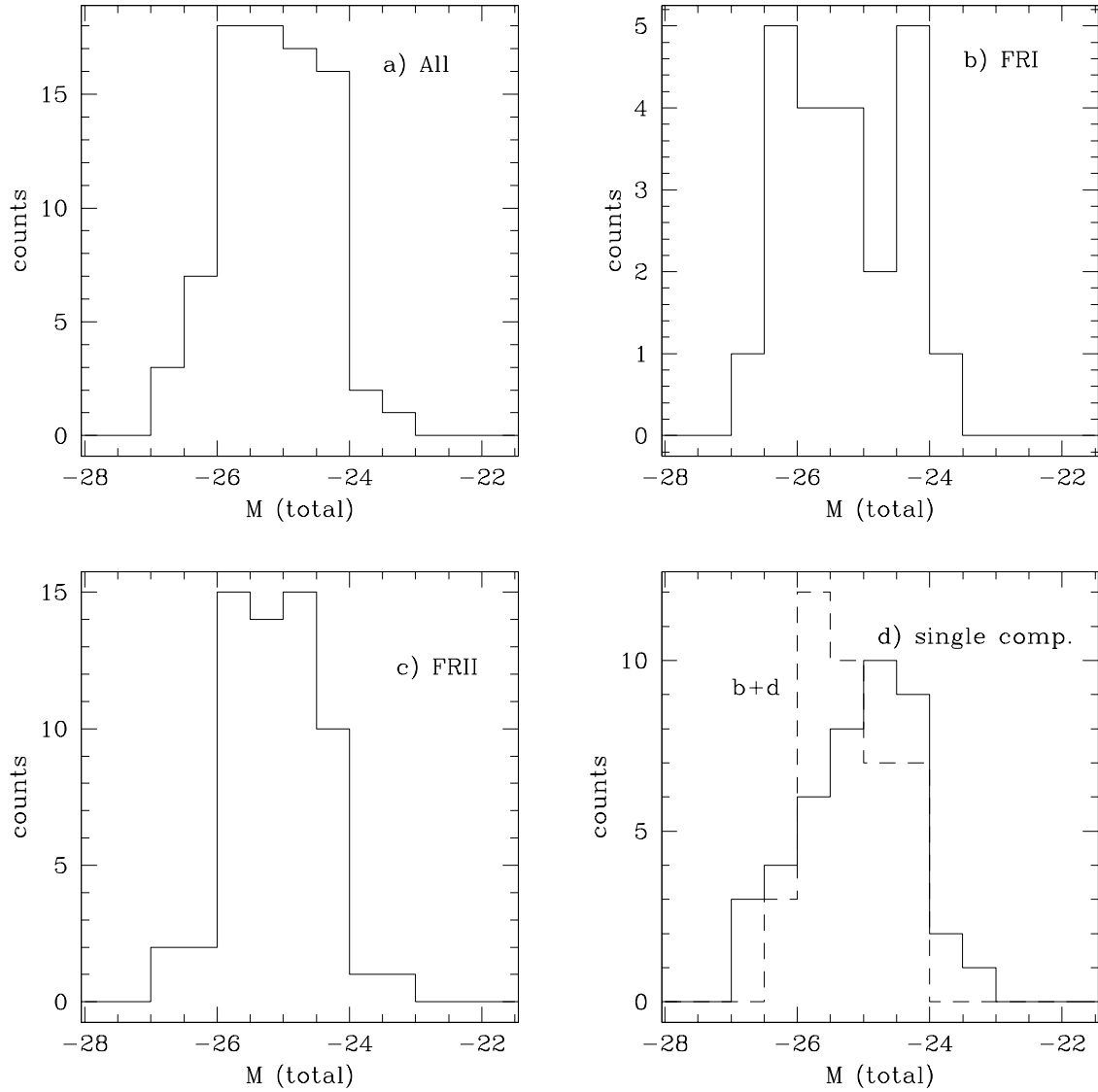


Fig. 3.— Total luminosity distributions for: a) Whole sample, b) FR I galaxies, c) FR II galaxies, d) Galaxies with single Sérsic luminosity profile (solid line histogram) and for bulge+disk luminosity profile galaxies (dashed line histogram).

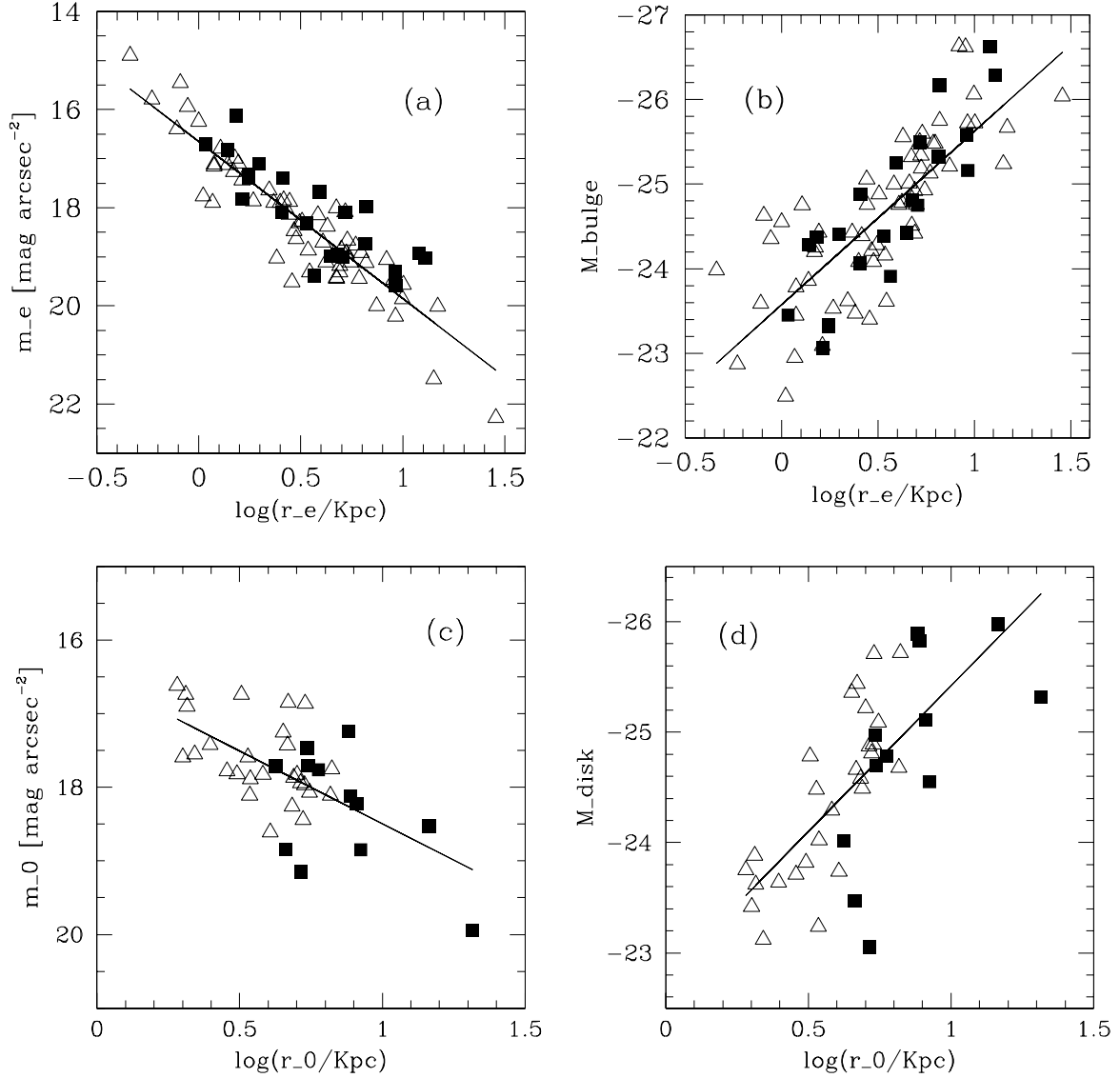


Fig. 4.— Photometric correlations: a) Effective magnitude vs. log of the effective radius, b) bulge luminosity vs. log of the effective radius, c) central surface magnitude vs. log of the length scale, d) disk total luminosity vs. log of the length scale. Squares represent FR I galaxies while empty triangles represent FR II galaxies. Lines show the result of the linear regression.

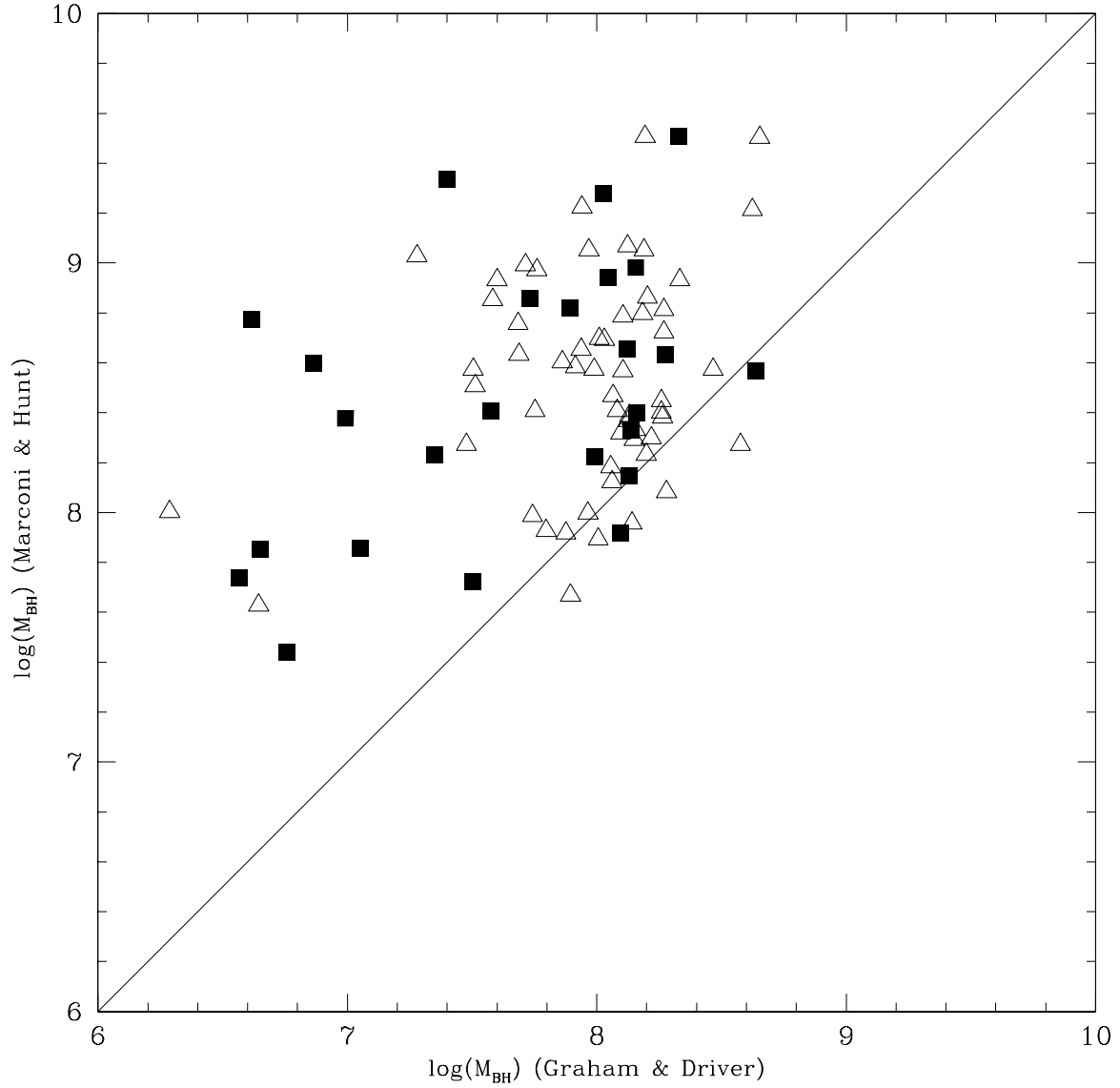


Fig. 5.— Black hole masses calculated for the sample galaxies. X-axis show the results obtained using the Graham & Driver (2006) relation while y-axis show masses obtained following the Marconi & Hunt (2003) relation. Squares and empty triangles represent FR I and FR II galaxies respectively. Solid line indicates the $y = x$ function.

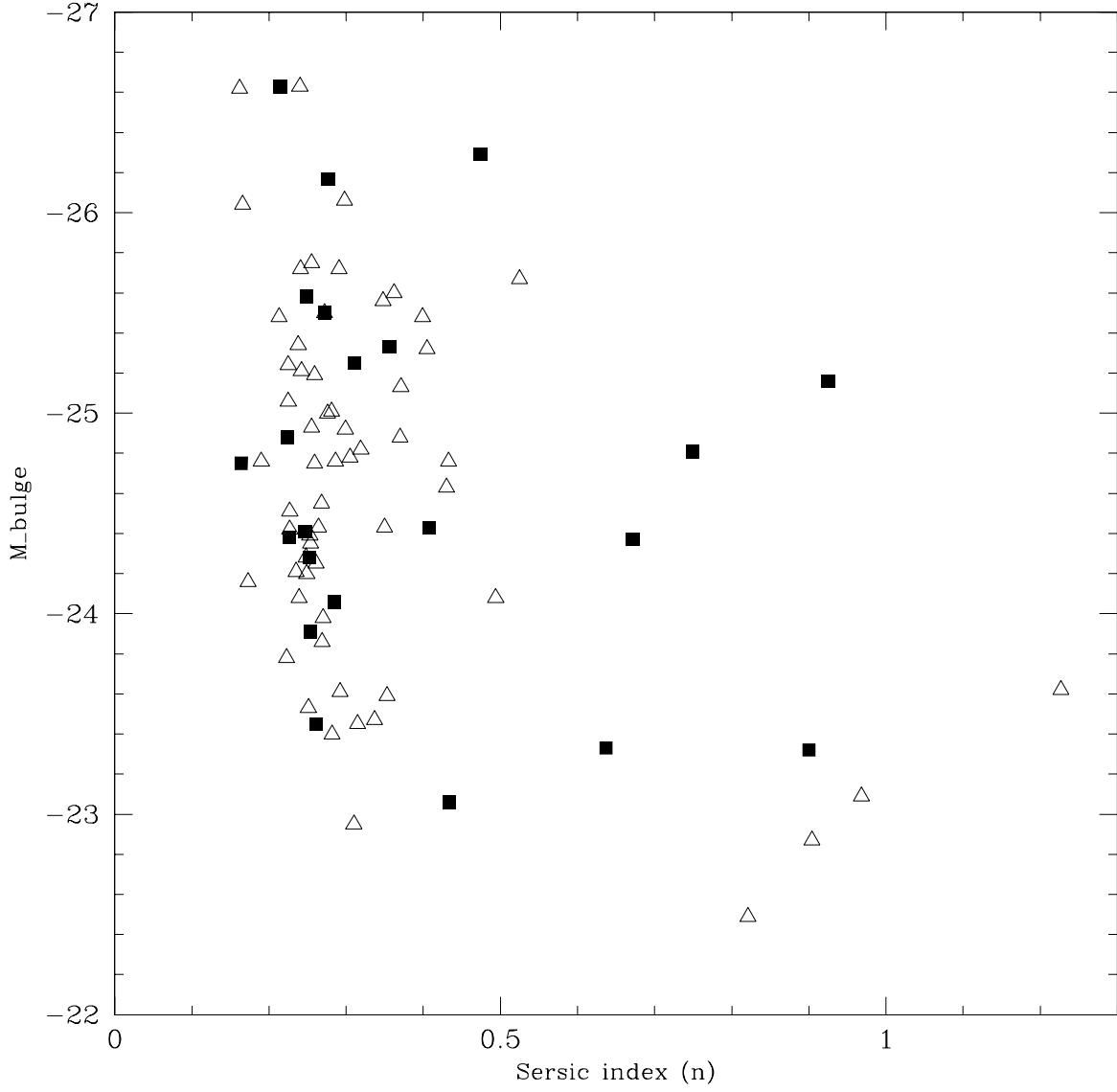


Fig. 6.— Total bulge luminosity versus Sérsic index n . Squares and empty triangles represent FR I and FR II galaxies respectively.